Journal of Materials Chemistry A

ROYAL SOCIETY OF CHEMISTRY

PAPER

View Article Online
View Journal

Cite this: DOI: 10.1039/d6ta02609e

Remote plasma polymers of iron(II) phthalocyanine in polyacrylonitrile-derived carbon electrospun fibres as electrodes for supercapacitors

Jose M. Obrero, *[a] Jorge P. V. Tafoya, [b] Michael Thielke,[b] G. P. Moreno-Martínez,[a] Lidia Contreras-Bernal,[ac] Jose Ferreira de Sousa, Jr,[a] Juan Ramón Sánchez-Valencia, [a] Angel Barranco [a] and Ana B. Jorge Sobrido *[b]

Remote plasma-assisted vapour deposition under nitrogen (RPAVD-N_2) is introduced as a single-step, solvent-free, room-temperature strategy to integrate iron(II) phthalocyanine (FePc) into carbon nanofibre (CNF) scaffolds for high-performance pseudocapacitive electrodes. In this process, CNFs are activated by low-energy N_2 remote plasma and subsequently exposed to sublimated FePc, which undergoes controlled plasma polymerization to form conformal, nitrogen-rich FePc-derived coatings while preserving Fe–N coordination. By tuning the plasma power, the degree of crosslinking, defect generation and molecular fragmentation are precisely controlled. Structural and spectroscopic analyses reveal progressive incorporation of amine, nitrile and oxygenated functionalities while maintaining the Fe–N coordination environment, with 30 W power providing the optimal balance between structural integrity and defect density. Plasma processing enhances the capacitance by nearly one order of magnitude compared to sublimated FePc films, underscoring the critical role of plasma-induced molecular integration. The FePc30W@CNFs electrode delivers 80.9 F g^{-1} at 0.25 A g^{-1} (areal capacitance of 0.79 F cm^{-2} at 4.9 mA cm^{-2}), achieves 7.42 Wh kg^{-1} at 225 W kg^{-1}, and retains 86.5% of its initial capacitance after 6000 cycles. These results demonstrate that remote plasma polymerization enables robust, high-rate and durable phthalocyanine-based electrodes, establishing RPAVD as a scalable platform for next-generation energy-storage materials.

Received 26th March 2026
Accepted 1st June 2026

DOI: 10.1039/d6ta02609e

rsc.li/materials-a

1. Introduction

The rapidly increasing demand for clean, efficient, and reliable energy storage technologies has become a critical challenge in the context of integrating renewable energy sources. In parallel, the rise of portable and wearable devices has highlighted the need for energy storage systems that can handle rapid cycling and high-power demands, beyond the capabilities of conventional batteries.[1] Supercapacitors have emerged as promising candidates to address this challenge, offering long cycle life, high power density, ultrafast charge–discharge capability, low maintenance costs, eco-friendliness, and exceptional cycling stability.[2] Nevertheless, their relatively low energy density compared to batteries continues to limit their broader implementation, driving intense research efforts toward advanced electrode materials and architectures. Based on their energy storage mechanisms, supercapacitors can be classified into electric double-layer capacitors (EDLCs) and pseudocapacitors.[3] The nature, structure, and accessibility of the electrode active materials fundamentally govern the electrochemical performance of supercapacitors. Carbon-based materials, including activated carbons, carbon nanotubes, and graphene derivatives, dominate both commercial and academic research owing to their high surface area, excellent electrical conductivity, and robust rate capability.[4–6] However, their charge-storage mechanism is primarily based on electric double-layer capacitance, which intrinsically restricts the achievable capacitance and energy density. In contrast, pseudocapacitors rely on fast and reversible surface or near-surface faradaic reactions, enabling substantially higher capacitance. Representative pseudocapacitive materials include transition-metal oxides,[7] conductive polymers,[8] and redox-active molecular systems.[9] Despite their promise, these materials often suffer from limited electrical conductivity, inefficient utilisation of electroactive sites, structural degradation upon cycling, and difficulties in

[a]Nanotechnology on Surfaces and Plasma Laboratory, Materials Science Institute of Seville (CSIC-US), C/ Américo Vespucio 49, 41092, Seville, Spain
[b]Centre for Sustainable Engineering, School of Engineering and Materials Science, Faculty of Science and Engineering, Queen Mary University of London, Mile End Road, London, E1 4NS, UK
[c]Química-Física, Department of Physical Chemistry, University of Seville, C/Professor García González no 2, Seville 41012, Spain. E-mail: jmanuel.obrero@icmse.csic.es; a.sobrido@qmul.ac.uk

achieving homogeneous and stable coupling with conductive carbon matrices.[10,11] To overcome these limitations, composite electrode architectures combining conductive carbon frameworks with pseudocapacitive components have been widely explored, aiming to synergistically merge high electrical conductivity, large surface area, and enhanced redox activity. However, in most reported composites, the pseudocapacitive phase is physically mixed, weakly anchored, or heterogeneously distributed, which frequently results in poor electrical coupling, inefficient utilisation of molecular active sites, and limited long-term electrochemical stability. Therefore, developing composite electrodes that enable controlled, conformal integration of pseudocapacitive species within a conductive carbon network, independent of the specific material class, remains a critical challenge.[12]

Within this broader context, redox-active molecular systems integrated within conductive carbon frameworks represent an attractive subclass of pseudocapacitive materials.[9] In such hybrid architectures, the molecular units provide discrete redox-active centres, while the carbon scaffold ensures fast charge transport and mechanical stability. Among these molecular systems, metal phthalocyanines have gained increasing attention in recent years.[13–15] These complexes exhibit reversible metal-centred redox chemistry and an extended π-conjugated structure that facilitates efficient charge transfer and surface-confined faradaic reactions. Electrochemical studies have shown that phthalocyanine-based electrodes can display characteristic pseudocapacitive behaviour, including quasi-rectangular voltammetric profiles, high rate capability, and good reversibility. To date, the incorporation of metal phthalocyanines into carbon-based electrodes has relied primarily on wet-chemical routes, physical mixing, or post-synthetic assembly, among others.[13,16–18] Although these approaches enable the introduction of molecular redox units into conductive matrices, they frequently result in heterogeneous molecular distribution, aggregation-induced loss of electroactive sites, and weak interfacial electronic coupling. Moreover, multistep fabrication procedures and harsh thermal or chemical treatments can compromise the intrinsic molecular structure of phthalocyanines, causing partial loss of metal-nitrogen coordination and reduced long-term electrochemical stability. As a result, current strategies offer limited control over molecular-level integration and interfacial chemistry, restricting the efficient utilisation of redox-active centres and hindering reproducible device performance. In parallel, plasma-based techniques have been increasingly explored for the fabrication and modification of supercapacitor electrode materials, owing to their ability to tailor surface chemistry, introduce heteroatom doping, engineer defects, and deposit functional coatings under solvent-free and low-temperature conditions.[19,20] Most reported plasma approaches have focused on the synthesis or activation of carbonaceous materials, including activated carbons, carbon nanotubes, graphene derivatives, and vertically aligned nanostructures.[21] Plasma processing has also been employed for the deposition of inorganic pseudocapacitive phases such as transition-metal oxides and nitrides.[22] However, despite the extensive use of plasma technologies in supercapacitor research, their application to the molecular-level integration of redox-active phthalocyanines into conductive carbon frameworks remains remarkably limited. In particular, plasma-enabled strategies capable of immobilising molecular pseudocapacitive units in a conformal and stable manner, while preserving their metal–nitrogen coordination environment and intrinsic redox activity, have been scarcely explored. Nevertheless, plasma-assisted strategies reported so far have not demonstrated the direct, single-step, solvent-free and room-temperature integration of metal phthalocyanines into conductive carbon frameworks, remaining largely limited to surface activation, etching, or partial molecular modification rather than controlled molecular immobilisation.

In this work, we introduce a novel plasma-enabled methodology based on remote plasma-assisted vapour deposition (RPAVD),[23–28] using nitrogen plasma to fabricate molecularly integrated pseudocapacitive electrodes based on iron(II) phthalocyanine (FePc) films. In this continuous single-reactor process, a carbon nanofibre (CNF) freestanding scaffold is initially exposed to a low-energy remote nitrogen plasma, resulting in surface activation and nitrogen functionalisation of the conductive carbon network. Subsequently, FePc molecules are sublimated into the downstream plasma region, where they undergo controlled plasma polymerization to form nitrogen-rich plasma polymers conformally deposited onto the pre-functionalised carbon surface. This sequential dual functionality, achieved within a single uninterrupted plasma process, enables intimate interfacial coupling and enhanced electrical connectivity between the redox-active plasma polymer and the carbon scaffold. In this configuration, the carbon framework primarily contributes electric double-layer capacitance and electronic conductivity, whereas the FePc-derived plasma polymer introduces fast surface-confined faradaic reactions, together resulting in a hybrid pseudocapacitive electrochemical capacitor behaviour. Importantly, RPAVD is a solvent-less room-temperature process fully compatible with thermally or chemically sensitive substrates. By carefully tuning the plasma–molecule interaction, this strategy allows the immobilisation of FePc-derived plasma polymers with different degrees of polymerization, preserving the Fe–N coordination environment and its intrinsic redox activity, while simultaneously promoting defect engineering and interfacial stability within the carbon framework. Compared to sublimated FePc, the plasma-polymerised electrodes exhibit a nearly tenfold increase in capacitance in some cases, demonstrating that plasma processing not only enables molecular immobilisation but also fundamentally enhances pseudocapacitive performance. Using FePc as a model system, we demonstrate that RPAVD converts fragile molecular redox units into robust pseudocapacitive composite electrodes exhibiting high capacitance, excellent rate capability, and remarkable cycling stability. Beyond this specific case, the present work establishes remote plasma polymerization as a general and versatile platform for the single-process fabrication of molecularly engineered pseudocapacitive electrodes for next-generation energy storage devices. To the best of our knowledge, this work represents the first demonstration of a remote plasma-assisted strategy for the controlled molecular

integration of phthalocyanines into conductive carbon frameworks for pseudocapacitive energy storage applications.

2. Experimental

2.1 Synthesis of CNFs from polyacrylonitrile by electrospinning

9.5 wt% polyacrylonitrile (PAN, M_W 150 kDA, Sigma Aldrich) and 0.5 wt% carbon black (C) (99.9%, 75 m^2 g^{-1}, Alfa Aesar) were dissolved in DMF (>99.9%, Fisher) overnight. Electrospinning was performed at 24 kV positive voltage and a flow rate of 0.5 mL h^{-1} in a standard horizontal setup with a grounded collector at a tip-to collector distance of 15 cm (Fig. 1a). A total of 8 mL was spun to obtain the PAN/C fibres (CNFs), which were subsequently activated in a preheated box furnace for 2 h at 200 °C and finally carbonised in a tube furnace at 900 °C for 4 h in a N_2 atmosphere with a heating rate of 5 °C min^{-1} to obtain the final carbon nanofibres (CNFs).

2.2 Deposition of FePc plasma polymer thin films by remote plasma assisted vapour deposition (RPAVD)

Iron(II) phthalocyanine (FePc, with a dye content > 90%) was purchased from Sigma-Aldrich and utilised without further purification. CNF samples were positioned within an ECR-MW plasma reactor (Fig. 1b) operating at 2.45 GHz, between the plasma discharge and the Knudsen sublimation cell, with the CNFs facing away from the glow discharge (the CNF-to-glow-discharge distance is 6 cm, and 12 cm in the most remote plasma-induced deposition). In addition to CNF electrodes, clean flat substrates of silicon (Si (100)) and fused silica were placed alongside the CNFs inside the reactor. These planar substrates served as reference supports to evaluate the morphology and optical properties of the FePc plasma polymer films under identical deposition conditions. Before initiating plasma processes, the reactor was evacuated to a base pressure of approximately 10^{-6} mbar. The CNFs were then subjected to an N_2 plasma pretreatment at 240 W for 30 minutes to generate surface defects and incorporate nitrogen-containing functionalities. The nitrogen flow was dosed with a calibrated mass flow controller set at 30 sccm. The gas pressure was controlled *via* an automated butterfly valve regulator, which controls the pumping flow of the system to maintain a pressure of 10^{-2} mbar. Immediately after pretreatment, FePc molecules were sublimated under N_2 plasma conditions with different plasma powers and geometrical configurations. During FePc sublimation, the working pressure was kept at 10^{-2} mbar. The experimental parameters selected for nitrogen plasma polymerization, including plasma power, treatment distance from the sublimation cell, and relative position to the glow discharge, and the sample labels assigned to each condition, are summarised in Table 1.

The 30 W condition corresponds to the minimum power at which a stable N_2 plasma can be ignited in our reactor, enabling deposition in the mildest plasma environment. The powers 30,

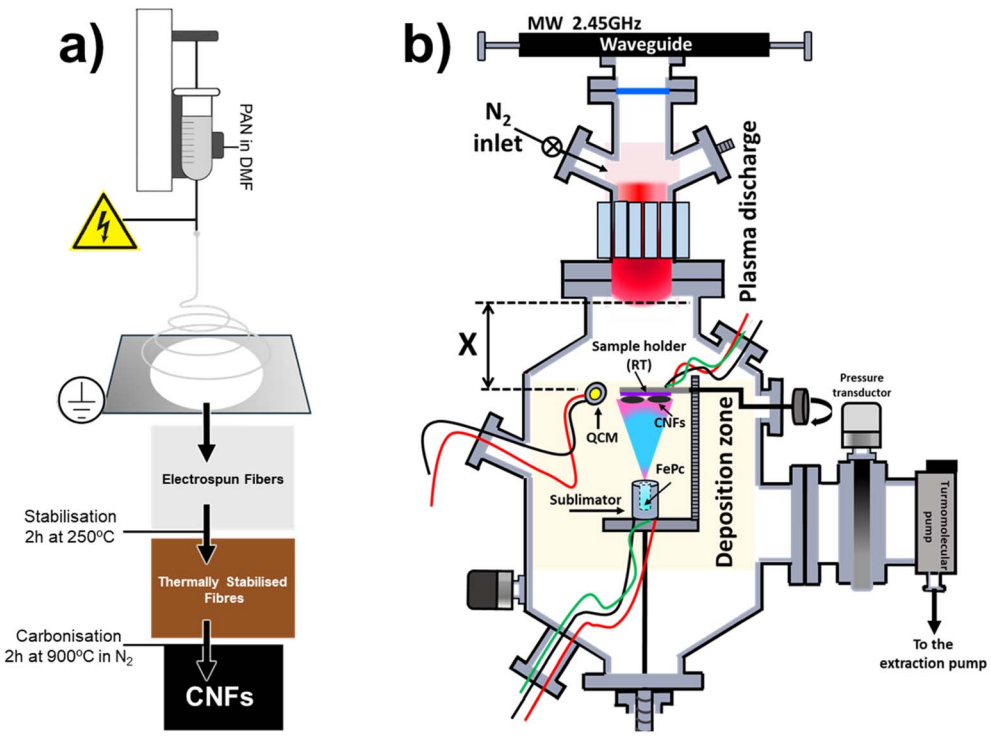

Fig. 1 Schematic representation of the fabrication process for FePc plasma polymers@CNFs. (a) Schematic of the conventional electrospinning process for preparing CNFs. A droplet of PAN/C dissolved in DMF is subjected to a high electric field, producing a charged jet that is accelerated toward a grounded collector. The resulting fibre mat is removed, thermally stabilised, and carbonised to obtain CNFs. (b) Schematic of the RPAVD reactor used for plasma-assisted polymerization of FePc.

Table 1 Experimental conditions employed for the conformal deposition of FePc remote plasma polymers and sublimated films

Sample label	N_2 plasma power (W)	$d_{sample\text{-}sublim.}$[a] (cm)	$d_{sample\text{-}glow}$[a] (cm)
Sublimated FePc (FePcSubl)	0	9	—
FePc 30W-3 cm	30	3	12
FePc 30W	30	9	6
FePc 60W	60	9	6
FePc 240W	240	9	6

[a] $d_{sample\text{-}sublim.}$ and $d_{sample\text{-}glow}$ indicate the distance between the sample and the sublimation cell and the sample and the glow discharge region, respectively.

60 and 240 W were selected to represent low, intermediate (×2) and high (×8) plasma activation regimes, allowing a systematic comparison of their effect on the polymer structure and electrochemical performance. The deposition rate and resulting thickness of each FePc were monitored using a quartz crystal microbalance (QCM) placed near the sample holder. The temperature of the Knudsen cell was adjusted to maintain a constant growth rate of 0.5 Å·s^{-1} (density of 0.5 g cm^{-3}, and *z*-factor of 1.0 in the QCM electronics). The substrates remained at room temperature throughout deposition, as measured by an encapsulated thermocouple connected to the sample holder, which was unaffected by the plasma discharge. To ensure uniform plasma polymer coverage across the entire CNF network, including fibres located deeper within the porous architecture, the samples were flipped after the first deposition step. A second deposition was then performed on the previously shadowed reversed side under identical plasma conditions, resulting in homogeneous coating on both faces of the fibrous electrodes and throughout the three-dimensional network. In addition, the CNF substrates received the same N_2 plasma pretreatment on the hidden face before FePc deposition, as described above, so that both sides of the electrodes were functionalised under equivalent conditions.

2.3 Characterisation methods

High-resolution field emission scanning electron microscopy (FESEM) images of the samples deposited on CNFs and silicon wafers were obtained in a Hitachi S4800 field emission microscope, working at 2 kV. Cross-sectional views of the flat substrates were prepared by cleaving the Si (100) wafers before imaging. Compositional changes were analyzed by using Energy Dispersive X-ray (EDX) spectra obtained with a Bruker-X Flash-4010 analyzer working at 20 kV installed in the same SEM system. Transmission electron microscopy (TEM), selected-area electron diffraction (SAED) and scanning transmission electron microscopy (STEM) analyses were performed using a Tecnai G2 F30 S-Twin microscope. Portions of the samples were mechanically scraped from the substrates and transferred onto Cu grids coated with a lacey carbon support film. STEM-EDX spectroscopy was used to examine the elemental distribution of the FePc plasma polymer coatings.

Optical transmittance properties of the samples deposited on fused silica substrates have been analyzed in the 200–1500 nm wavelength range, using a PerkinElmer Lambda 750 S UV–vis–NIR spectrophotometer. The spectral resolution was 2 nm.

Raman spectroscopy measurements were performed using a Renishaw inVia confocal Raman microscope equipped with a 20× objective lens and a 633 nm red laser, operated at 50% of its nominal power. Each spectrum was acquired with five accumulations to improve the signal-to-noise ratio. *In situ* Raman characterization of the electrospun mats was carried out using a dedicated electrochemical Raman cell (MTI Corporation, EQ-STC-Raman). In these experiments, the applied potential of the supercapacitor assembly was held until equilibrium was reached prior to spectral acquisition. The charging process was investigated by increasing the potential from an initial value of 0.00 V in equidistant steps of 0.1 V up to 0.75 V (last step of 0.05 V). For the discharging process, the same procedure was followed by decreasing the applied potential from 0.75 V back to 0.00 V. The spectral resolution for this configuration was ~1.6 cm^{-1}. No polarisation was applied during the experiments.

XPS characterisation studies were performed using a Scientific Nexsa X-ray photoelectron spectrometer. The spectra were collected in the pass energy constant mode at 50 eV using a monochromated Al Kα X-ray source. The C1s signal at 284.8 eV was used to calibrate the binding energies (BEs). High-resolution spectra of individual elements (C 1s, N 1s, O 1s, Fe 2p, and K2p) were collected with 50 accumulations to improve the signal-to-noise ratio. Peak assignments were performed according to values reported in the literature.[29,30]

Electrochemical measurements (cyclic voltammetry, CV; chronopotentiometry; and electrochemical impedance spectroscopy, EIS) were performed using a supercapacitor assembly in a quick-assembly split cell (MTI Corporation, EQ-HSTC, 20 mm diameter). The full-cell assembly was connected to a Biologic SP300 potentiostat. For the physical assembly of the supercapacitor, two disks of 0.6 cm diameter were punched from the electrospun mats coated with plasma-polymerised FePc (FePc@CNFs). A third disk of equal diameter was cut from Whatman Grade GF/D Glass Microfibre Prefilters, and used as the electrolyte reservoir. This separator disk was soaked overnight in 6 M KOH solution to ensure full impregnation with the electrolyte. Prior to assembly, the soaked separator was gently drained to remove excess solution. The final cell configuration consisted of a symmetric stack: FePc@CNFs/electrolyte-soaked separator/FePc@CNFs, compressed within the EQ-HSTC cell. The mass used for the calculation of the gravimetric capacitance corresponds to the total mass of the active electrode (CNFs + FePc samples) in the symmetric configuration. The mass of each electrode disk was measured using an analytical precision balance (±0.01 mg accuracy) prior to cell assembly. No subtraction of the pristine CNF mass was applied, as the performance of the full composite electrode was evaluated. For completeness, and to isolate the contribution of the FePc coatings, its areal mass loading was independently quantified by Rutherford Backscattering Spectrometry (RBS). Since RBS

was performed on isolated plasma-polymer films, the obtained values correspond exclusively to the FePc coatings and not to the full CNF-based electrode. The resulting mass loadings for each plasma condition are reported in Table S1 in the SI.

3. Results and discussion

3.1 Characterisation of the FePc plasma polymers

In the RPAVD technique, the solid precursor is sublimated into the downstream region of a microwave plasma discharge, where it interacts with reactive species under remote plasma conditions. As a result, the molecules are not fully fragmented, and a substantial proportion of intact or partially dissociated precursor units becomes incorporated into a growing polymeric film.[23–27,31,32] This process provides a versatile and solvent-free route to immobilise transition-metal macrocycles on conductive substrates at room temperature. Unlike our previously reported plasma polymerization studies that used argon as the working gas,[23–27,31,32] the present work employs nitrogen (RPAVD-N_2). The use of N_2 plasma is particularly advantageous because it can promote the nitridation or nitrogen functionalisation of specific sites on the CNF substrates, improving the interaction between the plasma polymer and the carbon matrix. The degree of interaction between the plasma and the precursor, defined here as the polymerization degree, can be tuned by adjusting the plasma power. In the present work, this parameter was varied between 30 and 240 W, together with the control of the distance between the sample and glow discharge (denoted as X in Fig. 1b, see also Table 1), allowing the systematic study of its effect on the structural, chemical, and electrochemical properties of the resulting FePc plasma polymers.

The SEM images of the RPAVD-N_2 samples on CNFs obtained at different polymerization degrees (including the sublimated one) are shown in Fig. 2. The as-prepared CNFs (Fig. 2a) exhibit a smooth and clean surface with almost no visible roughness. The slight surface irregularities observed are mainly attributed to the preliminary N_2 plasma exposure, a routine pretreatment that introduces surface defects and nitrogen-containing functional groups, thereby enhancing surface reactivity and adhesion of the subsequent FePc coating. A comparison of the CNFs before and after the N_2 plasma pretreatment is presented in Fig. S1. The direct sublimation of FePc produces a polycrystalline conformation (Fig. 2b) with randomly oriented grains formed by the metallic complex molecules. The RPAVD of FePc onto the CNFs generates smooth samples with almost inappreciable features at the nanoscale (Fig. 2c–e). In all these cases, the N_2 plasma promotes the formation of a uniform shell surrounding each CNF, showing excellent homogeneity in thickness from the top to the bottom of the fibres. To further verify the compositional uniformity of the plasma-polymerised coatings, EDX elemental mapping was performed (Fig. S2). The spatial distributions of C, N, O and Fe closely follow the morphology of the carbon nanofibres, confirming a continuous and conformal coverage along the entire fibre surface under all RPAVD-N_2 conditions. At low plasma power (30 W), the FePc plasma polymer displays a rougher and more granular morphology, particularly evident in the film deposited on the Si substrate (Fig. 2f). A statistical distribution of CNF diameters at different RPAVD powers is shown in Fig. S3. Using the diameter distributions referenced to the N_2 pretreated CNFs (209.7 ± 24.7 nm), the coating thicknesses can be estimated as ~151 nm for the sublimated film, ~56 nm at 30 W, ~31 nm at 60 W and ~115 nm at 240 W. An analogous evolution is observed for the thin films deposited on Si, whose thickness decreases from 565 ± 11 nm (sublimated) to 163 ± 5 nm (30 W) and 105 ± 7 nm (60 W), with a slight increase to 125 ± 8 nm at 240 W. Although the magnitude of these variations is not identical between the flat and fibrous geometries (owing to intrinsic differences in surface area, curvature and the degree of exposure to plasma-activated species), the consistency in the overall growth pattern indicates that both systems undergo the same transitions between fragmentation-dominated, activation-dominated and redeposition-assisted regimes characteristic of plasma-assisted

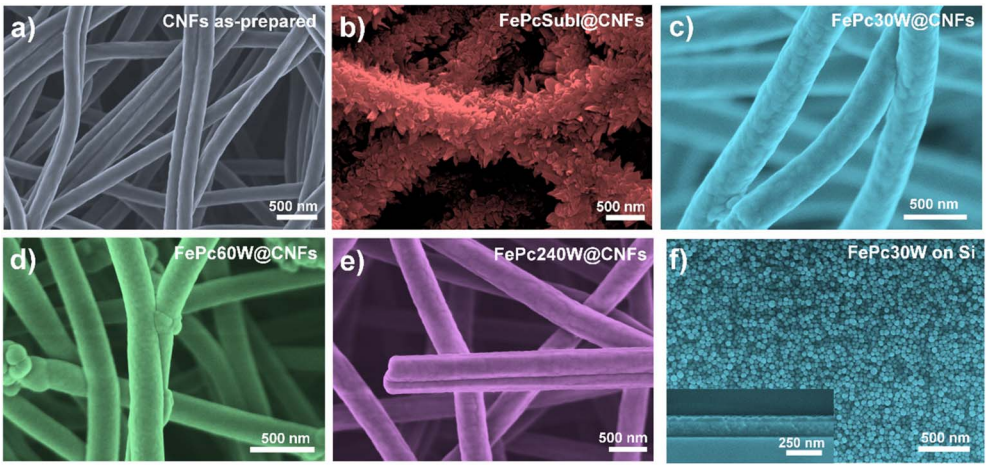

Fig. 2 SEM micrographs of the CNF-based systems obtained by deposition of FePc by RPAVD-N_2 at different polymerization degrees. (a) CNFs; (b) CNFs coated with FePc by sublimation; (c) RPAVD at 30 W; (d) at 60 W; (e) at 240 W; and (f) top-view of the FePc deposited on a flat (silicon) substrate by RPAVD at 30 W. The inset of (f) shows the corresponding cross-sectional view of the same film.

polymer growth. In all cases, the relatively narrow diameter dispersions demonstrate the high uniformity of the conformal coating along the fibre length. The granular morphology observed at 30 W indicates a limited interaction between the FePc precursor and the plasma, enabling the deposition of only partially polymerised species and precursor crystallites. Increasing the plasma power to 60 W and 240 W progressively smooths and compacts the surface, consistent with enhanced molecular fragmentation and crosslinking. The stronger interaction with the N_2 plasma promotes greater precursor activation and film densification, yielding a more homogeneous and continuous layer. Overall, these results show that higher plasma power increases the degree of FePc polymerization, producing denser but less molecularly defined coatings, as observed in the film on the Si(100) substrate shown in Fig. S4.

TEM analysis (Fig. S5) was performed to examine the internal structure of the coated fibres. The images show a representative example of carbon nanofibres uniformly covered by the plasma-polymerised FePc layer, with a continuous shell clearly distinguishable around each fibre. The selected-area electron diffraction (SAED) pattern exhibits a diffuse halo, confirming the fully amorphous nature of the plasma-polymerised coating. No crystalline domains are detected within the deposited layer, indicating that the RPAVD process produces an amorphous plasma polymer rather than molecularly crystalline FePc. STEM-EDX analysis also reveals the presence of Fe associated with the fibre surface, providing direct evidence of the FePc-derived material conformally covering the CNFs.

The optical response and molecular integrity of the FePc plasma polymers were analysed by UV-vis-NIR spectroscopy (Fig. 3a). The sublimated FePc film shows the characteristic absorption bands of iron(II) phthalocyanine, with a Q band at 621 nm (Q-band region) accompanied by a small shoulder at 564 nm, and a B/Soret band at 315 nm, confirming the preservation of the molecular structure.[33,34] Upon plasma polymerization *via* RPAVD-N_2, these spectral features progressively diminish in intensity and undergo bathochromic shifts as the plasma power increases. In the FePc 30W-3 cm sample, both the Q and B/Soret bands remain nearly unchanged compared to the sublimated film, suggesting minimal disruption of the FePc macrocycle. However, at higher plasma powers, notably in the FePc 240W sample, the Soret band shifts markedly to 663 nm, accompanied by a significant reduction in intensity and complete loss of the B band. This spectral evolution reflects a gradual loss of molecular order and π-conjugation, as well as the possible partial oxidation of the central iron atom. Although a decrease in molecular conjugation typically reduces electronic delocalisation, in plasma-polymerised FePc this effect promotes the formation of a more defect-rich and chemically heterogeneous network. Such structural disorder increases the density of electrochemically accessible Fe–N_x sites and facilitates charge-transfer pathways at the CNF interface, thereby providing a direct link between the reduced π-conjugation observed in the UV–vis spectra and the enhanced pseudocapacitive performance of the FePc@CNFs electrodes.

These changes indicate a transition from a well-defined molecular material (intact FePc) to a crosslinked and partially delocalized plasma polymer network. In contrast to the sublimated FePc film, which undergoes progressive degradation upon air exposure, all plasma polymer films retain their optical integrity over time. This enhanced environmental stability is an intrinsic feature of plasma polymers and makes them particularly suitable as protective and functional coatings.[31,35] Evidence of this effect is presented in Fig. S6a, where the sublimated FePc film exhibits the appearance of a shoulder at ≈710 nm after 1300 days of air exposure, indicative of oxidation and molecular degradation.[36,37] Conversely, the RPAVD-N_2 30W plasma polymer (Fig. S6b) shows no detectable spectral changes after the same period, confirming its remarkable long-term stability.

Raman spectra of the thin films of the FePc sublimated and plasma polymer films deposited on CNFs (FePc@CNFs) are presented in Fig. 3b. The characteristic D band (~1336 cm^{-1}),

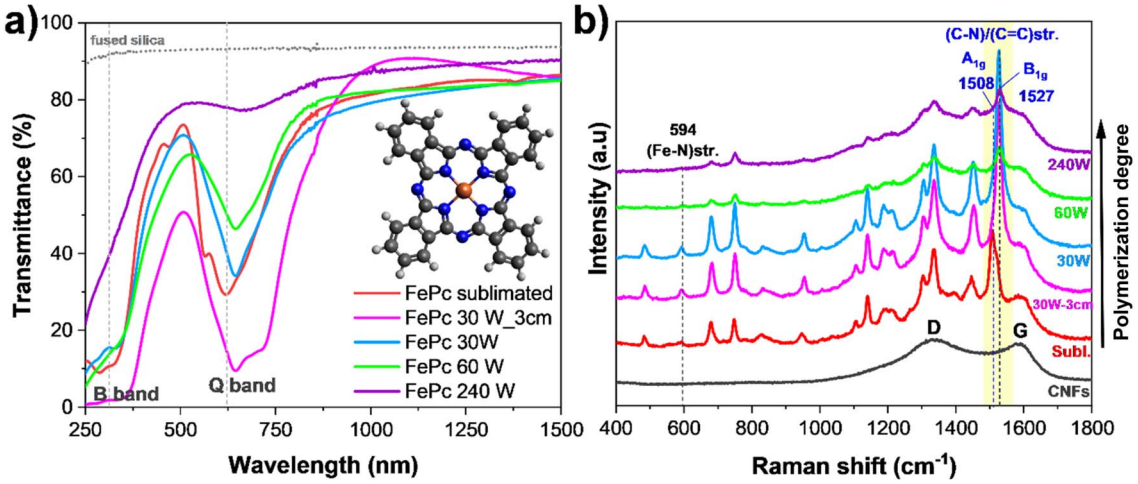

Fig. 3 (a) UV–vis–NIR transmittance spectra of FePc thin films deposited on fused silica, comparing sublimated samples with those plasma-polymerised *via* RPAVD-N_2 at different degrees of polymerization. (b) Raman spectra of FePc@CNFs samples at varying polymerization degrees, including the reference spectrum of bare CNFs.

corresponding to the A_{1g} breathing mode of defective C_6 ring vibrations, and the G band (~1586 cm^{-1}), attributed to the E_{2g} stretching mode of sp^2 carbon, are clearly observed.[38] The intensity ratio I_D/I_G is approximately 1.10, indicating a high degree of structural disorder within the fibres. This value exceeds the typical range reported for similar systems, where I_D/I_G ratios generally fall between 0.75 and 0.81,[39] which suggests that the increased disorder is attributed to the mild N_2 plasma pretreatment applied to the fibres. The in-plane crystallite size (coherence length, L_a) was estimated using the modified Tuinstra–Koenig relation (eqn. (1)):[40,41]

$$L_a(\mathrm{nm}) = 2.4 \times 10^{-10} \lambda_{\mathrm{nm}}^4 \left(\frac{I_D}{I_G}\right)^{-1} \quad (1)$$

where λ is the laser wavelength of 633 nm, yielding a coherence length of $L_a \approx 35$ nm. This value indicates that nanocrystalline graphitic domains are preserved within the CNFs despite the relatively high defect density reflected by the I_D/I_G ratio, evidencing a defect-rich but still conductive graphitic framework. Therefore, the plasma treatment does not destroy the graphitic structure but introduces additional defects and edge sites, increasing surface reactivity while maintaining efficient electron transport pathways. In addition, a significant broadening of the D band is observed, suggesting a wide distribution of graphene-like domain sizes and elevated structural heterogeneity.[42] This phenomenon supports the hypothesis that plasma exposure induces controlled fragmentation of the graphitic network, resulting in a more reactive surface architecture. Collectively, these effects are expected to enhance ion adsorption and, consequently, improve the specific capacitance of the material. In this context, the defect-rich carbon framework generated by plasma exposure provides a larger population of edge sites, vacancies and heteroatom-coordinated environments that act as electrochemically active centres. These defects facilitate charge transfer and increase the accessibility of Fe–N_x redox sites within the FePc coating, establishing a direct link between the Raman signatures of structural disorder and the enhanced pseudocapacitive behaviour of the FePc@CNFs electrodes.

The $FePc_{sublimated}$@CNFs sample (red spectrum) shows the fingerprint Raman bands of iron(II) phthalocyanines.[43,44] Among its main signals, the band at 594 cm^{-1} is associated with Fe–N stretching, confirming the coordination of the metal centre within the macrocycle. Other relevant peaks are found at 482, 680, 750, 832, 950, 1140, 1187, 1306, 1336, and 1452 cm^{-1}, corresponding to vibrational modes of the macrocyclic ring, mainly C–N and C=C stretching and in-plane deformation modes. In the high-wavenumber region, two prominent bands appear at 1508 and 1527 cm^{-1}. According to the literature, these features correspond to symmetry-allowed skeletal vibrations of the phthalocyanine macrocycle, namely the totally symmetric A_{1g} mode (1508 cm^{-1}) and the B_{1g} mode (1527 cm^{-1}), both arising from collective C–N/C=C stretching of the isoindole and benzene rings rather than from distinct local functional groups.[43,44] In well-ordered crystalline FePc films, the higher-frequency B_{1g} mode at around 1530–1540 cm^{-1} is typically the most intense and is often used as a marker of the metallophthalocyanine framework.[45,46] In contrast, the $FePc_{sublimated}$@CNFs shows a dominant contribution at 1508 cm^{-1} ($I_{1508}/I_{1527} \approx 3.0$), indicating a relative enhancement of the totally symmetric A_{1g} mode. This behaviour can be attributed to the disordered molecular arrangement and substrate interaction in the sublimated layer, which relax Raman selection rules and modify the relative intensities of symmetry-dependent vibrational modes. After mild N_2 plasma treatment (30 W–3 cm and 30 W), a clear redistribution of intensity is observed: the 1527 cm^{-1} B_{1g} band becomes dominant and the I_{1508}/I_{1527} ratio drops to ~0.06. This change occurs due to a plasma-induced reduction of molecular symmetry and the initiation of crosslinking within the phthalocyanine network. At higher plasma power (60 W and 240 W), the 1527 cm^{-1} band remains predominant but becomes broader and less defined, indicating increased structural disorder and partial amorphisation due to excessive crosslinking. The Fe–N stretching band at 594 cm^{-1} remains visible in all samples, confirming that the Fe centre stays coordinated and that no demetalation occurs during plasma processing. Overall, mild plasma polymerization induces a controlled reorganisation of the FePc macrocycles, whereas stronger plasma conditions lead to a loss of long-range order without disrupting the metal–nitrogen coordination, anticipating the electrochemical behaviour discussed in the following section.

The surface chemical composition of sublimated FePc and plasma-polymerised FePc films deposited on CNFs, and pristine CNFs was analysed by X-ray photoelectron spectroscopy (XPS). The corresponding survey spectra and the atomic percentages of each element are shown in Fig. 4a and f, respectively. As the degree of plasma polymerization increases, the films exposed to the N_2 plasma show a progressive increase in the relative nitrogen content compared to the sublimated FePc film. Starting from an $(N/C)_{sublimated}$ ratio of 0.15, close to that expected from the empirical formula of FePc ($C_{32}H_{16}N_8Fe$), the N/C ratios of the plasma polymer films increase to $(N/C)_{30W\text{-}3cm} = 0.23$; $(N/C)_{30W} = 0.28$; $(N/C)_{60W} = 0.33$ and $(N/C)_{240W} = 0.50$. This trend confirms the effective incorporation of nitrogen into the polymeric matrix as the plasma–precursor interaction becomes stronger, while the overall carbon content gradually decreases. In all samples, a certain amount of oxygen is also detected. In the case of the sublimated FePc film, the oxygen traces are attributed to mild surface oxidation upon air exposure after deposition and water adsorbed on the surface. For the plasma polymer films, however, the higher oxygen content is a characteristic feature of any plasma-assisted process, such as RPAVD. Residual oxygen may be incorporated from the reactor atmosphere during deposition, as well as from post-deposition reactions of dangling bonds and trapped radical species with ambient air.[24,31] On the other hand, the amount of atomic Fe remains nearly constant for all samples, close to 1 at%, indicating that the plasma treatment does not lead to significant loss or sputtering of iron. These global trends already suggest that plasma exposure progressively enriches the films in nitrogen- and oxygen-containing functionalities.

As shown in Fig. S7, N_2 plasma pretreatment significantly modifies the surface chemistry of the CNFs, increasing the relative amount of pyrrolic-N species. This nitrogen enrichment

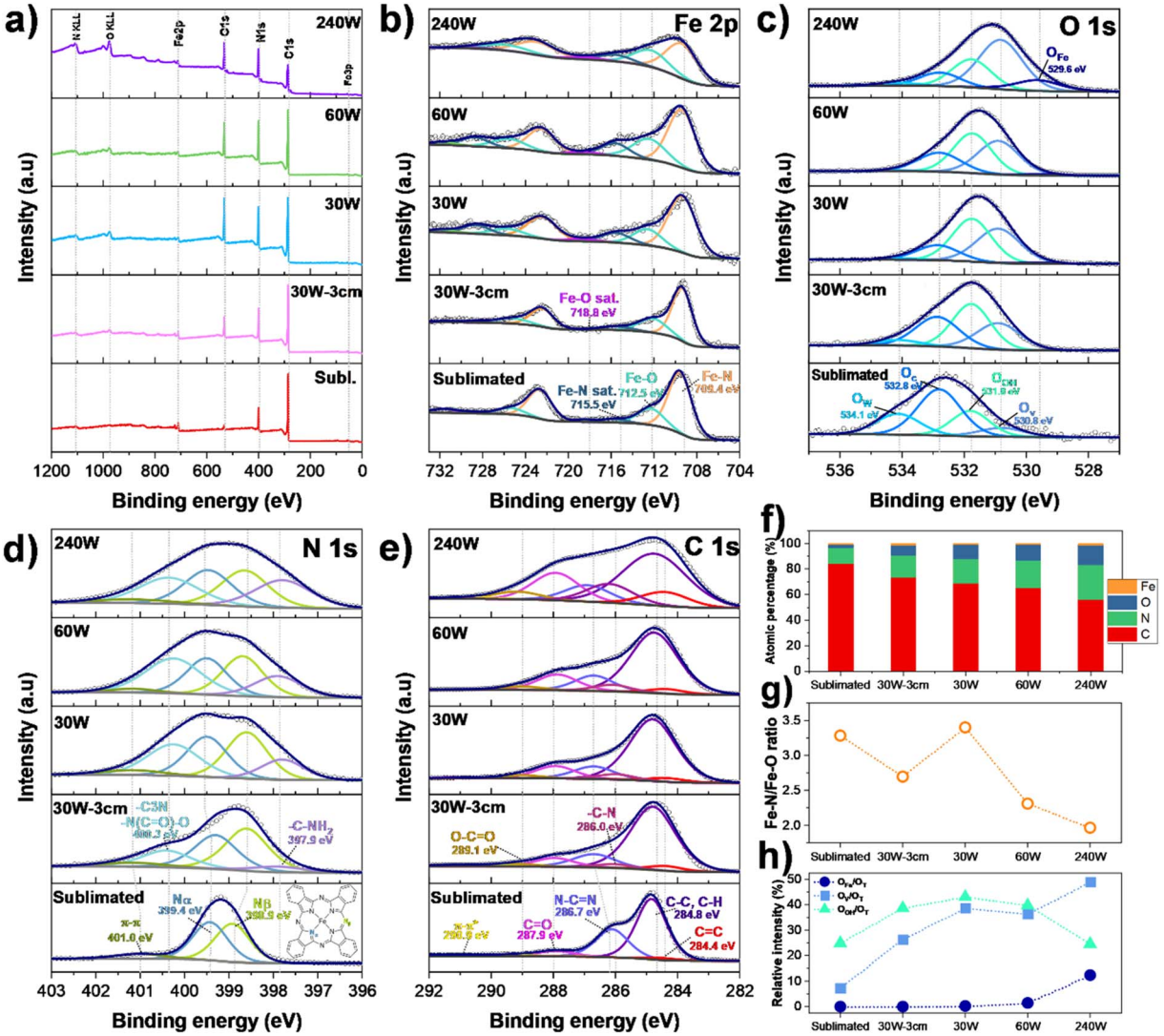

Fig. 4 (a) XPS survey spectra of the sublimated FePc and the plasma-polymerised samples at different degrees of polymerization *via* RPAVD. Detailed high-resolution spectra of (b) Fe 2p; (c) O 1s; (d) N 1s and (e) C 1s regions. (f) Surface atomic percentages of the films determined by XPS. (g) Fe–N/Fe–O ratio as a function of polymerization degree extracted from the Fe 2p region. (h) Relative contributions of O_{Fe}, O_v and O_{OH} species with respect to the total oxygen content (O_T), obtained from the deconvolution of the O 1s spectra.

indicates a soft-etching process that generates reactive carbon sites subsequently functionalized by N_2 species.[47] These modifications are expected to influence FePc coordination during deposition.

To evaluate the chemical evolution of FePc at different RPAVD polymerization degrees, high-resolution XPS spectra of the Fe 2p, O 1s, N 1s and C 1s regions were analysed (Fig. 4). The Fe 2p region shows that plasma power primarily controls the oxidation state of iron while preserving Fe–N coordination under moderate conditions. Fig. 4b shows the XPS spectra corresponding to the Fe 2p region, whose deconvolution reveals two main components common to all samples: a peak at 709.4 eV attributed to Fe^{2+} coordinated to nitrogen atoms of the phthalocyanine macrocycle (Fe–N), and a second peak at 712.5 eV associated with Fe^{3+} species, resulting from partial oxidation of Fe^{2+} to Fe^{3+} (Fe–O),[48–50] as well as their spin–orbit counterparts separated by 13.1 eV. The Fe–N/Fe–O ratios (Fig. 4g) reveal that the 30 W sample preserves the Fe^{2+} coordination within the phthalocyanine macrocycle most effectively, whereas higher plasma powers progressively increase Fe–O formation, indicating stronger oxidation. This trend is corroborated by the O 1s spectra (Fig. 4c), which show contributions from O_{Fe}, O_V, O_{OH}, O_C and O_W.[26,51] The O_{Fe} component at 529.6 eV increases with power, consistent with enhanced Fe oxidation. The peak at 530.8 eV (O_V) corresponds to oxygen vacancies, which create defect sites that may favour charge transport but also indicate structural disorder when excessive. Moderate vacancy concentrations have been reported to enhance conductivity, ion transport and the density of electrochemically active sites.[52,53] In contrast, the O_{OH} peak at 531.8 eV rises sharply at high powers, reflecting excessive surface hydroxylation and partial passivation. The O_C component at

532.8 eV corresponds to oxygen bound to carbon atoms in oxidized organic groups (C═O and –O–C═O), reflecting the partial oxidation of the phthalocyanine polymer backbone. Finally, the peak at 534.1 eV (O_W) is attributed to molecular water adsorbed on the surface. The relative ratios O_{Fe}/O_T, O_V/O_T and O_{OH}/O_T (Fig. 4h) confirm that the 30 W condition provides the best compromise between controlled oxidation, defect creation and surface stability. These oxygen species indicate that plasma treatment introduces controlled defect sites while excessive power leads to surface over-oxidation. The N 1s spectra (Fig. 4d) of sublimated FePc exhibit the expected pyridinic (N_β) and pyrrolic (N_α) components, whose nearly identical integrated areas reflect the characteristic 1 : 1 abundance of these nitrogen environments in the phthalocyanine macrocycle, together with the typical π–π satellite.[24,54] Plasma interaction induces small shifts while preserving the N_α/N_β ratio, indicating that the phthalocyanine macrocyclic framework is largely preserved. Two new components at 397.9 and 400.3 eV grow with increasing plasma power, arising from primary amines, nitriles, tertiary amines, and oxidised nitrogen species generated during plasma-driven fragmentation and reorganisation.[26,55,56] However, the strong overlap of nitrogen species in this region prevents an unambiguous assignment of the 400.3 eV peak, which likely reflects a mixture of amine, nitrile and oxidised nitrogen groups formed partly through secondary reactions with residual oxygen. This evolution reflects the enhanced incorporation of amine-, nitrile- and oxygen-containing nitrogen species, indicating plasma-induced fragmentation and reorganisation of the FePc framework. These structural transformations are expected to influence the capacitive behaviour of the films, linking the plasma-induced chemical evolution directly to the electrochemical response discussed in the following section. The formation of additional nitrogen functionalities increases the density of electrochemically active sites and improves electronic interaction with the CNF substrate. Similarly, the C 1s spectra (Fig. 4e) evolve from the characteristic FePc structure to increasingly nitrogen- and oxygen-functionalised carbon environments. The C═N-related peak shifts by +0.6 eV due to reduced electron density, and two new peaks appear at 286.1 and 289.0 eV, corresponding to C–N groups and to oxygen-rich carbon species, respectively,[57,58] confirming the incorporation of amine, nitrile and oxidised groups. Since the binding energies of C–N and C═N overlap in the 285.9–287.0 eV range, their distinction in the C 1s spectra is not straightforward; therefore, the assignments were confirmed through the N 1s region, which more clearly reveals the formation of amine and nitrile groups under plasma exposure. These chemical modifications enhance interfacial charge transfer and increase the density of electroactive sites, contributing to the improved pseudocapacitive response of the plasma-polymerised samples. In summary, XPS demonstrates that RPAVD-N_2 plasma processing simultaneously preserves Fe–N coordination, introduces nitrogen-rich functionalities and generates controlled oxygen-related defects, while partially disrupting the phthalocyanine framework. The 30 W condition provides the optimal balance between structural integrity and defect density, directly explaining the superior electrochemical performance of FePc30W@CNFs.

The electrochemical performance of each FePc-coated CNF (FePc@CNFs) film was evaluated using a two-electrode system in 6 M KOH aqueous solution. To demonstrate the capacitive behaviour of each sample, cyclic voltammetry (CV) and galvanostatic charge–discharge (GCD) measurements were compared. The electrochemical performance of the bare CNFs pre-treated with N_2 plasma is shown in Fig. S8. The CNFs display a nearly rectangular CV curve, indicating that energy storage occurs predominantly through electric double-layer capacitance.[39] Fig. 5a shows the CV response (the final voltammogram out of ten recorded) for each sample, measured at a scan rate of 10 mV s^{-1}. As observed, the voltammogram of the FePcsublimated@CNFs sample (red trace) does not exhibit capacitive behaviour, displaying well-defined oxidation/reduction peaks within the studied potential window (0.00–0.75 V), characteristic of faradaic battery-type processes. These results are consistent with the XPS data, which indicate redox deactivation of FePc due to Fe–CNF coordination. The complete electrochemical performance of the $FePc_{sublimated}$@CNFs is presented in Fig. S9. Following RPAVD polymerization, this behaviour is no longer observed within the same potential range, and the resulting voltammograms become nearly rectangular, with the current remaining almost constant throughout the sweep and no discernible peaks. This response is consistent with pseudocapacitive behaviour, where charge storage arises from fast, reversible surface redox reactions rather than purely electrostatic double-layer formation. In metal phthalocyanines, this pseudocapacitive behaviour originates primarily from electron gain and loss at the central metal atom, and partly from proton absorption and desorption on pyridinic (N_β) or pyrrolic (N_α) nitrogen sites.[59] In the case of FePc, the high pseudocapacitance can be attributed to the pronounced redox activity of the central Fe, as illustrated in eqn (2):[60]

$$Fe^{2+}Pc \rightleftharpoons Fe^{3+}Pc + e^- \quad (2)$$

This intrinsic redox activity explains the reproducible pseudocapacitive performance observed across different FePc electrodes and supports the enhanced charge storage capability of the optimised plasma-polymerised samples.

Although this behaviour is observed in most polymerised samples, not all exhibit the same electrochemical performance. In particular, the FePc30W@CNFs (blue) and FePc30W-3cm@CNFs (pink) samples, synthesised at the same plasma power but at different glow-discharge distances, exhibit the most pronounced pseudocapacitive behaviour, with nearly rectangular voltammograms enclosing the largest areas. In contrast, increasing the plasma power leads to a gradual loss of charge-storage capability: the FePc60W@CNFs sample (green) already shows a reduced enclosed area, and this effect becomes even more pronounced in the FePc240W@CNFs sample (purple), whose voltammogram becomes narrower and more oval-shaped. This progressive decline in pseudocapacitance correlates with the XPS results, which reveal increasing Fe^{3+}

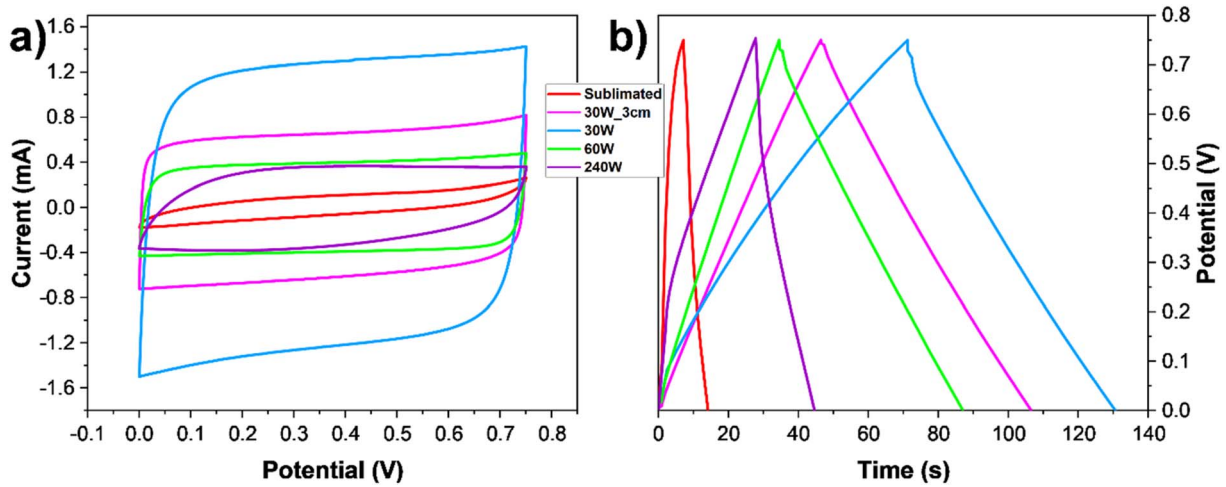

Fig. 5 Electrochemical performance of FePc@CNFs films. (a) Cyclic voltammetry curves recorded at a scan rate of 10 mV s^{-1}. (b) Galvanostatic charge–discharge profiles measured at a current density of 0.25 A g^{-1}.

content and diminished preservation of the Fe–FePc coordination environment.

Complementary insight into the capacitive behaviour was obtained from the GCD curves at 0.25 A g^{-1} shown in Fig. 5b. The $FePc_{sublimated}$@CNFs sample shows only a narrow, steep discharge profile, consistent with its poor capacitive response in CV. In contrast, the polymerised FePc@CNFs films exhibit nearly linear and symmetric triangular curves, confirming their pseudocapacitive behaviour and highly reversible redox processes. The longest discharge times are observed for FePc30W-3cm@CNFs and FePc30W@CNFs, in agreement with CV results and indicative of superior charge-storage capability. Increasing plasma power leads to shorter discharge times: the effect is already evident at 60 W and becomes more pronounced in FePc240W@CNFs, whose curve also deviates from linearity due to higher internal resistance. Overall, these results show that moderate plasma polymerization preserves the electroactive FePc structure while enhancing conductivity through the CNF network, whereas excessive power results in molecular degradation and performance loss.

Overall, the comparative electrochemical analysis indicates that FePc30W@CNFs is the most promising condition. Its combination of highly pseudocapacitive signatures in both CV and GCD, together with the favourable structural features revealed by XPS, indicates that moderate plasma polymerization at 30 W preserves the electroactive FePc environment while ensuring good electrical connectivity within the CNF network. Consequently, the following section focuses exclusively on FePc30W@CNFs, including its specific capacitance, cycling stability, and *in situ* Raman response under applied potential.

3.2 Electrochemical performance of FePc30W@CNFs samples

Fig. 6 summarises the electrochemical performance of the FePc30W@CNFs sample. The CV curves recorded at scan rates between 1 and 20 mV s^{-1} (Fig. 6a) retain a nearly rectangular shape, indicative of efficient pseudocapacitive behaviour. At higher scan rates (50 mV s^{-1}), however, the profiles progressively become more oval, reflecting increasing ion-diffusion limitations and a corresponding decrease in charge-storage efficiency. The total capacitance stored in an electrode arises mainly from two contributions: (1) the surface-controlled capacitive phenomenon, which includes both the faradaic pseudocapacitance caused by fast surface redox reactions and the non-faradaic double-layer charging (capacitive contribution), and (2) the diffusion-controlled capacitive process, in which ion diffusion into the bulk of the electrode plays a dominant role (diffusive contribution). To quantitatively analyse the relative contributions of these capacitive elements, a well-established deconvolution method was applied.[61–63] The current response of a pseudocapacitive electrode at a given potential can be expressed as the sum of a surface-controlled term, proportional to the scan rate v, and a diffusion-controlled term, proportional to $v^{1/2}$:[60]

$$i(v) = k_1 \times v + k_2 \times v^{1/2} \quad (3)$$

Here, the $(k_1 \times v)$ component includes both double-layer charging and fast surface-controlled pseudocapacitance, while the $(k_2 \times v^{1/2})$ term reflects the slower faradaic processes limited by ion diffusion into the electrode bulk. The results obtained from the least-squares fitting of the pseudocapacitive model at different scan rates are shown in Fig. 6b. The current values were extracted from the CV data at 0.4 V in the forward scan, a potential located within the pseudocapacitive region and free from redox peak interference. The excellent correlation between the model and the experimental data (Fig. 6c), with $R^2 = 0.9948$, confirms the reliability of the deconvolution approach and validates the separation of capacitive and diffusive contributions. Additional fits at 0 V, 0.4 V (reverse), and 0.75 V (Fig. S10) show the same behaviour, with equally high determination coefficients (see Table S2), demonstrating that the model (eqn (3)) is robust across the entire potential window. At low scan

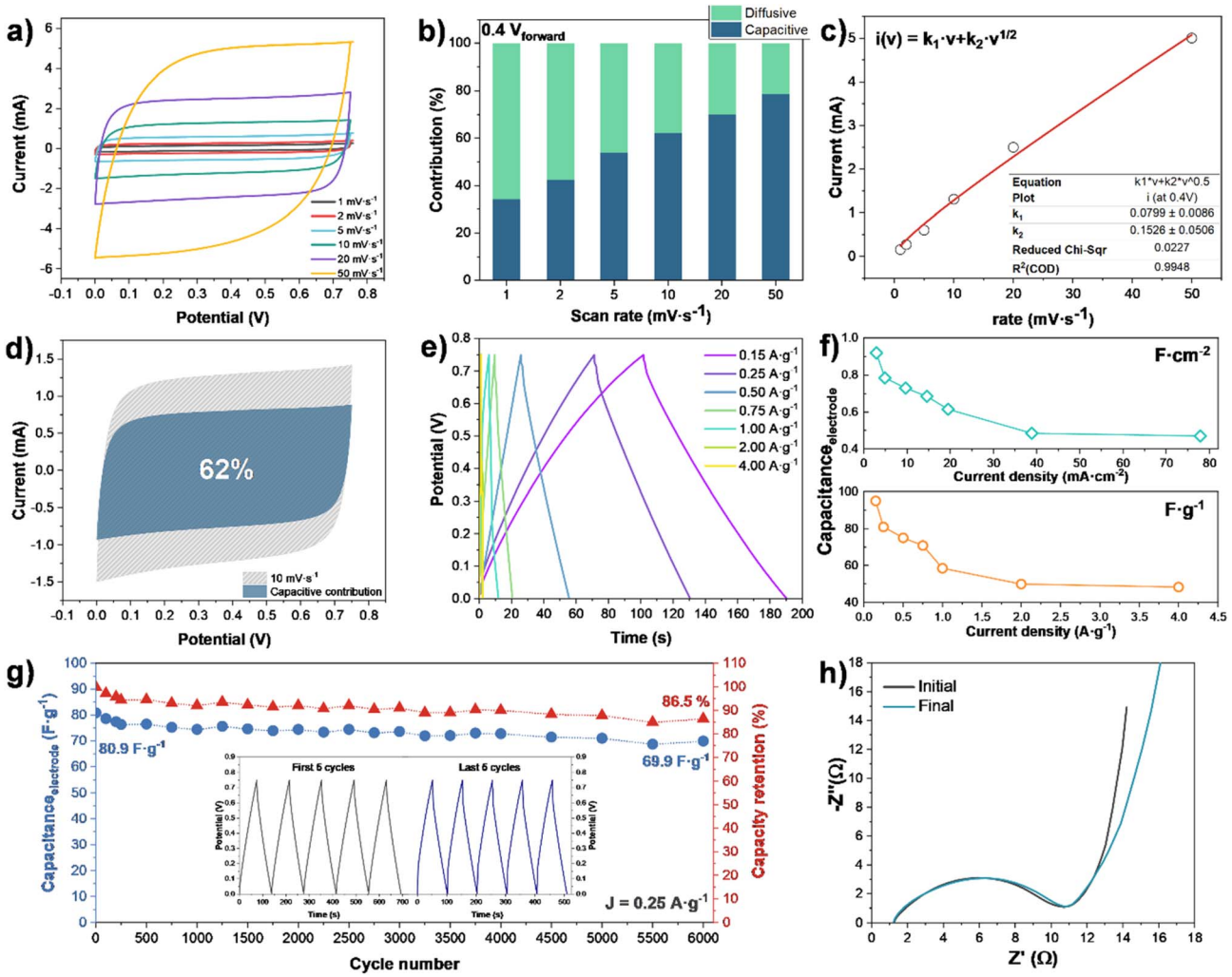

Fig. 6 Electrochemical performance of the FePc30W@CNFs sample. (a) CV curves recorded at scan rates ranging from 1 to 50 mV s^{-1}. (b) Capacitive and diffusive contributions at different scan rates, extracted using the pseudocapacitive current model. (c) Least-squares fitting of the model $i(v) = k_1 \times v + k_2 \times v^{1/2}$ applied to current data extracted from CV at 0.4 V in the forward scan. The inset displays the fitted k_1 and k_2 values along with the corresponding R^2. (d) CV curve at 10 mV s^{-1} highlighting the capacitive contribution. The shaded area is calculated according to eqn (2). (e) GCD curves recorded at various current densities. (f) Specific capacitance ($C_{electrode}$) expressed both gravimetrical (F g^{-1} *vs.* A g^{-1}) and areal (F cm^{-2} *vs.* mA cm^{-2}) as a function of current density. (g) Cycling stability and capacitance retention at 0.25 A g^{-1}. The inset shows the first and last five cycles during the stability test. (h) Nyquist plots recorded before and after cycling.

rates, the current is dominated by diffusion-controlled processes, as ions have sufficient time to penetrate the electrode bulk and participate in faradaic reactions. At higher scan rates, the capacitive component becomes dominant because the rapid potential sweep favours surface-controlled charge-storage mechanisms over ion diffusion. This transition is reflected in Fig. 6b–d, where the capacitive fraction reaches 62% at 10 mV s^{-1}, highlighting the major contribution of fast and reversible surface redox reactions in FePc30W electrodes. Fig. 6d further illustrates the contribution of surface capacitance to the total capacitance in the CV profile recorded at 10 mV s^{-1}, where the shaded region represents the capacitive fraction estimated from eqn (3). These design principles, including optimised nanostructures, active interfaces and accessible electroactive sites, are widely recognised as key factors governing pseudocapacitive behaviour. Such structure–property relationships are also observed in high-performance systems,[64,65] where rapid ion diffusion, efficient interfacial charge transfer nd abundant redox sites underpin their enhanced capacitance. In our system, the plasma-induced defect-rich FePc network and its intimate contact with the conductive CNFs follow the same principles, accounting for the improved pseudocapacitive response of the FePc30W@CNFs electrode.

The electrochemical performance was further examined through GCD measurements. Fig. 6e shows the GCD curves of the FePc30W@CNFs electrode at current densities from 0.15 to 4.0 A g^{-1} within the selected potential window. The profiles display an almost symmetric triangular shape, confirming the pseudocapacitive behaviour associated with fast surface-controlled faradaic reactions. The charging segments remain nearly linear, indicating rapid charge accumulation with minimal kinetic limitations, whereas the slight curvature

during discharge reveals the participation of slower diffusion-controlled processes. This asymmetry highlights the coexistence of surface pseudocapacitance and diffusion-limited ion release, fully consistent with the CV findings. The specific capacitance was then calculated from the discharge time, where the gravimetric capacitance of the symmetrical cell (C_{cell}) and the single electrode ($C_{electrode}$) is defined as:

$$C_{symCell(gravimetric)} = \frac{i \times \Delta t_{discharge}}{M_{total} \times \Delta V} \quad (4)$$

$$C_{electrode(gravimetric)} = 4 \times C_{symCell(gravimetric)} \quad (5)$$

where i is the discharging current, $\Delta t_{discharge}$ is discharging time, M_{total} represents the total mass of the two active electrode materials in the symmetric cell and ΔV is the potential window.[66] In addition, the areal capacitance of the electrode was calculated using the following expression:[67]

$$C_{electrode(areal)} = \frac{2 \times i \times \Delta t_{discharge}}{A_{electrode} \times \Delta V} \quad (6)$$

where $A_{electrode}$ is the geometric area of one electrode. The variation of specific capacitance with current density is presented in Fig. 6f. The FePc30W@CNFs electrode delivers 95.0, 80.9, 75.0, 70.8, 58.5, 49.9, and 48.3 F g^{-1} at current densities ranging from 0.15 to 4.00 A g^{-1}, corresponding to areal capacitances of 0.92, 0.79, 0.73, 0.69, 0.62, 0.49, and 0.47 F cm^{-2} at 2.9–77.9 mA cm^{-2}. These values far exceed those of the $FePc_{sublimated}$@CNFs electrode (8.5 F g^{-1} and 0.10 F cm^{-2} at 0.25 A g^{-1} and 3.1 mA cm^{-2}), representing an enhancement factor of ~9.5 and confirming the superior charge-storage capability of the plasma-polymerised films. Comparing both gravimetric and areal capacitances shows that the plasma-polymerised FePc coating clearly outperforms the sublimated FePc layer. Its higher capacitance and better rate capability arise from the improved conductivity and structural robustness of the plasma-polymerised network on the CNFs. Cycling stability is also a key parameter for evaluating the practical applicability of supercapacitors,[68] and was assessed through repeated GCD measurements (Fig. 6g). After 6000 cycles at 0.25 A g^{-1}, the FePc30W@CNFs electrode retains 86.5% of its initial capacitance, demonstrating excellent long-term durability. Comparable retentions of 86.1% and 87.5% at 0.50 and 1.00 A g^{-1}, respectively (Fig. S11), further confirm the robustness of the plasma-polymerised structure under high-rate operation. Impedance spectra recorded before and after cycling are shown in Fig. 6h. The Nyquist plots are characterized by a semicircle at high frequencies and a straight line at low frequencies. The semicircle is associated with the charge-transfer resistance at the electrode/electrolyte interface, while at low frequencies the diffusion process gives rise to a Warburg impedance with a 45° slope. As frequencies decrease, the line evolves into a (purely) capacitive response, shifting the phase angle from 45° to nearly 90°.[69,70] Before and after cycling, the semicircle remains essentially unchanged, while the Warburg line extends to lower frequencies toward the end of the cycling, demonstrating the excellent structural and interfacial stability of the FePc30W@CNFs electrode. For comparison, the electrochemical performance of the FePc60W@CNFs electrode is presented in Fig. S12, confirming the performance advantage of the 30 W condition.

Fig. 7 shows the XPS analysis of the FePc30W@CNFs electrode after 6000 charge–discharge cycles, revealing clear surface chemical changes. The survey spectrum evidences a strong alteration of the surface composition (C = 85.4%, N = 5.1%, O = 6.7%, Fe = 0.3%, and K = 2.5%), markedly different from the pristine film (C = 68.9%, N = 19.0%, O = 11.1%, and Fe = 1.0%) (Fig. 7b). The carbon enrichment and parallel decrease in N and Fe indicate partial loss or detachment of the plasma-polymer coating and exposure of bare fibres, as shown in Fig. S13. The appearance of K 2p features arises from KOH residues retained after rinsing.

Despite these changes, the high-resolution C 1s + K 2p spectrum (Fig. 7f) reveals that the main carbon functionalities, C=C (284.4 eV), C–C/C–H (284.8 eV), C–N (286.0 eV), N–C=N (286.5 eV), C=O (287.8 eV), O–C=O (289.0 eV), and π–π* interactions (291.1 eV) remain well defined, confirming that the carbon framework largely preserves its chemistry. A new component at 290.0 eV indicates the formation of potassium carboxylates (–COOK),[71] and the K $2p_{3/2}$ and K $2p_{1/2}$ peaks at 293.2 and 296.0 eV display the expected 2.8 eV spin–orbit splitting.[72]

In the N 1s region (Fig. 7e), the N_β/N_α ratio increases from 1.15 (pristine) to 2.4 after cycling, revealing a preferential loss of N_α species coordinated to Fe, which are more susceptible to OH^- attack in alkaline electrolyte. This selective degradation reduces Fe–N active sites, consistent with the moderate capacitance loss observed after long-term cycling. The Fe 2p spectrum (Fig. 7c) confirms that Fe–N coordination is largely retained, although the Fe^{3+}/Fe^{2+} ratio increases from 0.30 to 0.50 due to mild surface oxidation. This partial but not severe oxidation explains why the capacitance decreases gradually rather than abruptly. Finally, the O 1s spectra (Fig. 7d) show an increase in O_{Fe} and O_W, consistent with Fe oxidation and enhanced electrolyte/water retention. The increase in oxygen vacancy related contributions after cycling likely reflects electrochemically induced surface restructuring and dehydroxylation processes, which generate additional defect sites while preserving most Fe–N coordination. The partial coating detachment discussed above is mainly attributed to mechanical effects during post-cycling handling rather than to the electrochemical process itself. This structural reorganisation accounts for the gradual decline in capacitance observed during long-term cycling.

To further investigate surface structural changes during operation, *in situ* Raman measurements were performed. The experimental conditions and the measurement set-up are described in Section 2 and illustrated in Fig. S14. Fig. 8 shows the spectra collected during charging (a) and discharging (b). It can be noted that all Raman bands progressively attenuate upon charging, without noticeable shifts in peak position, reaching minimum intensity at 0.75 V. During discharge, the bands fully recover, confirming that the attenuation is a reversible physical effect rather than chemical degradation. The absence of peak

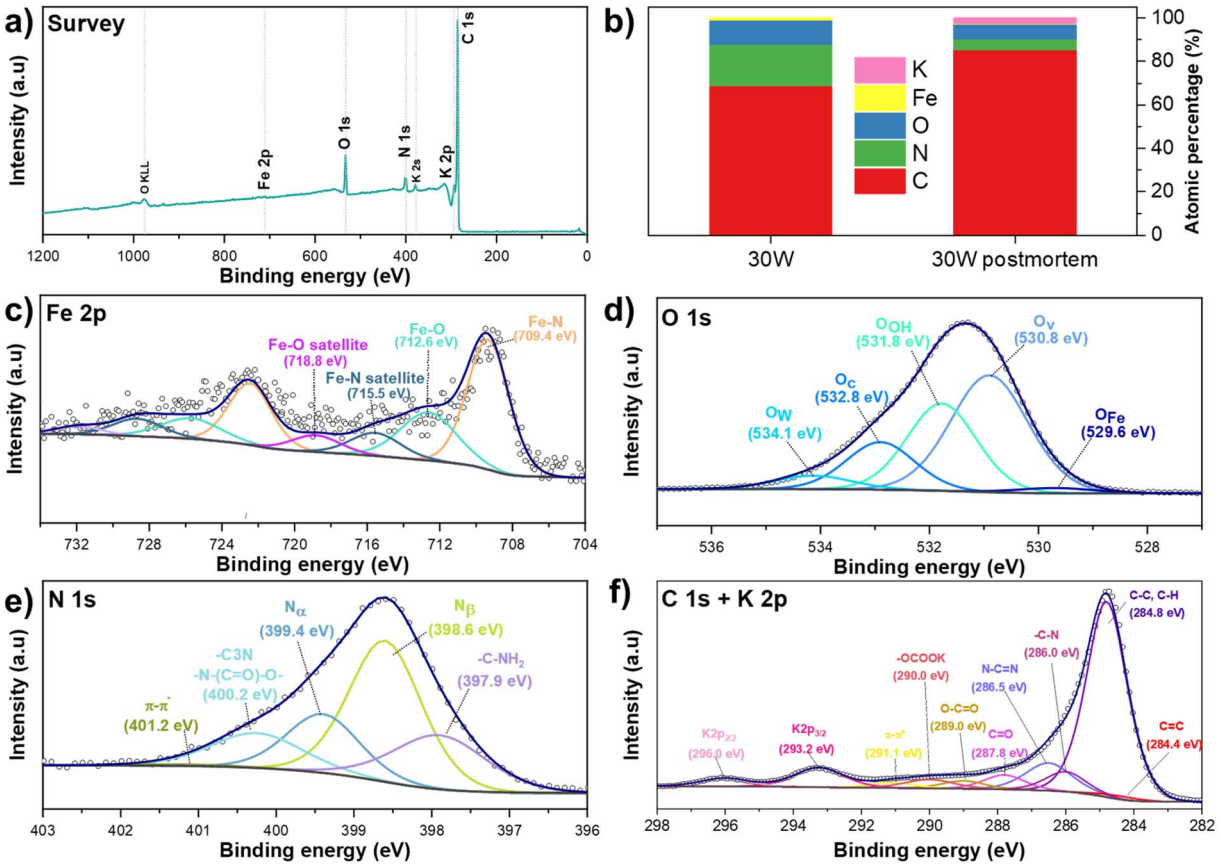

Fig. 7 (a) XPS survey spectra of the FePc30W@CNFs sample after 6000 charge–discharge cycles. (b) Surface atomic percentages determined by XPS, compared with those of the pristine FePc30W@CNFs film. Detailed high-resolution spectra of (c) Fe 2p; (d) O 1s; (e) N 1s and (f) C 1s + K 2p regions.

shifts or band broadening indicates that no significant structural transformation occurs, and the intensity modulation is instead attributed to reversible changes in the electronic structure under polarization. Variations in the charge density and oxidation state can modify the molecular polarizability, thereby affecting the Raman scattering efficiency without altering the vibrational framework. No new Raman features appear, in contrast with previous reports where irreversible oxidation or Fe^{2+} demetalation was observed.[43,73] Notably, the Fe–N stretching band at 594 cm^{-1} remains visible throughout the charge–discharge process, further confirming the stability of the metal–ligand coordination. Overall, the FePc30W@CNFs electrode responds to the applied potential through a reversible reorganization of its chemical environment while preserving structural integrity, fully consistent with the XPS results.

To benchmark the FePc30W@CNFs electrode against reported MPc-based systems, a Ragone plot was obtained, which relates energy density (Wh kg^{-1} or Wh cm^{-2}) to power density (W kg^{-1} or W cm^{-2}). The energy density of a single electrode is given by:[66]

$$E_{\text{electroded(gravimetric)}} = \frac{C_{\text{electrode}} \times \Delta V^2}{2 \times 3.6} \quad (7)$$

$$E_{\text{electroded(areal)}} = \frac{C_{\text{electrode}} \times \Delta V^2}{2 \times 3600} \quad (8)$$

where $C_{\text{electrode}}$ is the specific (gravimetric or areal) capacitance obtained from GCD curves, and ΔV is the potential window. The constants 3.6 and 3600 convert joules into Wh in gravimetric and areal units, respectively. The corresponding power density is defined as:[66]

$$P_{\text{electrode}} = \frac{E_{\text{electrode}}}{\Delta t} \times 3600 \quad (9)$$

Fig. 9 compares FePc30W@CNFs with previously reported MPc-based supercapacitors (FePc, CoPc, NiPc, CuPc and ZnPc), using literature-extracted energy/power values (full dataset in Table S3).[13,16–18,60,74–77] The blue star markers corresponding to FePc30W@CNFs were constructed from the energy and power densities calculated from individual galvanostatic charge–discharge (GCD) measurements at different current densities (0.15, 0.25, 0.50 A g^{-1}, *etc.*, see Fig. 6e); each point therefore represents a discrete experimental value rather than a fitted curve. The FePc30W@CNFs electrode achieves a high energy density of 7.42 Wh kg^{-1} at 225 W kg^{-1} (6.2×10^{-5} Wh cm^{-2} at 3.6×10^{-4} W cm^{-2}), and still delivers 0.85 Wh kg^{-1} at 6000 W kg^{-1}, demonstrating fast charge-transfer kinetics and excellent

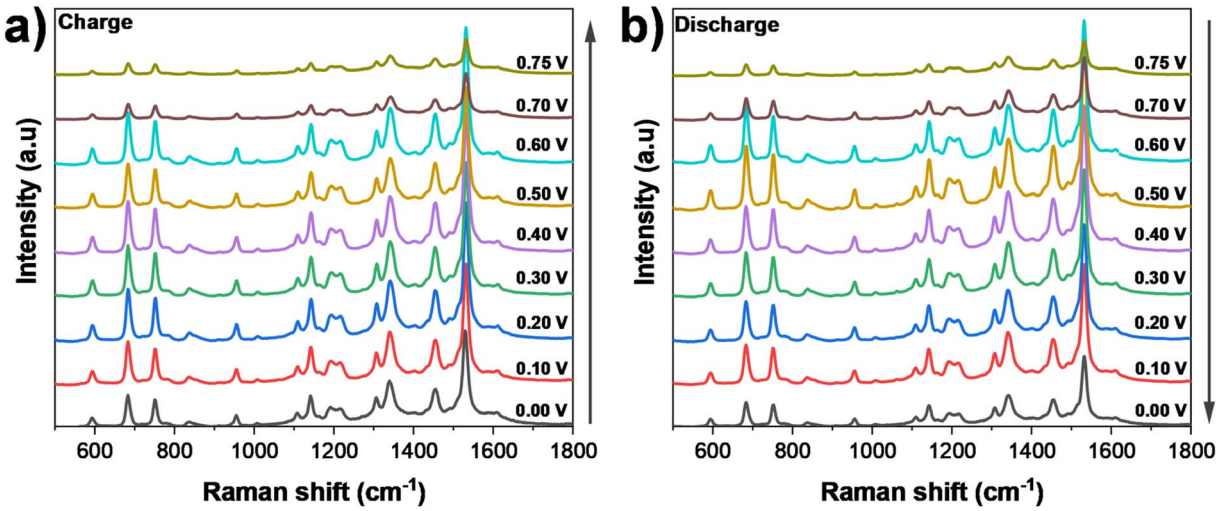

Fig. 8 *In situ* Raman spectra recorded under electrochemical potentiostatic conditions between 0 V and 0.75 V, during (a) charging and (b) discharging processes.

rate capability (8.2×10^{-6} Wh cm^{-2} at 0.06 W cm^{-2}). This Ragone profile highlights a stable energy-power balance across the full operating range.

Beyond MPc-based systems, recent reviews emphasise that state-of-the-art supercapacitors typically rely on the synergistic integration of conductive carbon scaffolds, defect-engineered or heterogeneous interfaces, and stabilised redox-active centres to enable fast ion/electron transport and high rate capability.[78,79] In this broader context, the FePc30W@CNFs electrode follows these contemporary design principles: the CNF network provides a highly conductive fibrous scaffold, while plasma-assisted polymerization generates defect-rich interfaces and preserves electroactive Fe–N coordination, supporting efficient pseudocapacitive kinetics. These results underscore the advantage of the RPAVD-N_2 plasma polymerization process, which stabilises the Fe–N electroactive centres while producing a nitrogen-rich, conductive and mechanically robust coating on CNFs. This synergistic architecture supports efficient pseudocapacitive reactions alongside rapid ion/electron transport, positioning FePc30W@CNFs as a high-performance, robust supercapacitor and confirming plasma-assisted polymerization as an effective strategy for energy-storage electrode engineering.

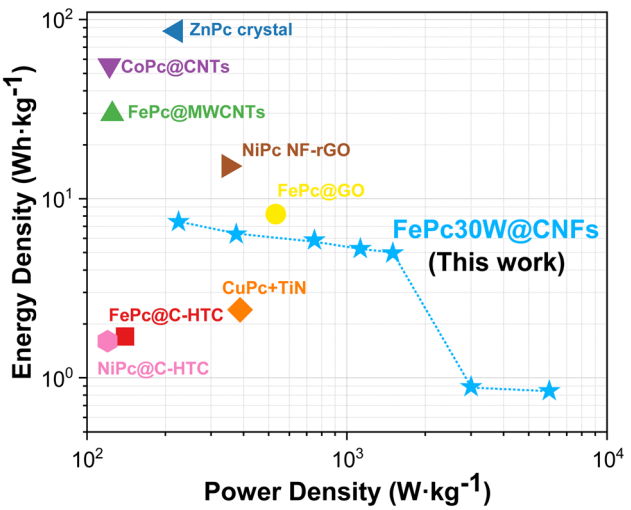

Fig. 9 Ragone plot comparing the FePc30W@CNFs electrode (blue star markers) with previously reported metal-phthalocyanine-based supercapacitors. The FePc30W@CNFs data points were obtained from energy and power densities calculated from individual GCD measurements at different current densities (see Fig. 6e).[13,16–18,60,74–77]

4. Conclusions

A novel methodology based on RPAVD of the iron(II) phthalocyanine plasma polymer using remote N_2 plasma was employed to fabricate FePc@CNTs electrode materials for supercapacitors. The remote N_2 plasma plays a dual role: it functionalises the as-prepared CNFs by introducing nitrogen-containing groups and defect sites, and simultaneously enables the plasma-assisted polymerization of FePc, forming a conformal coating with tuneable chemical composition. The RPAVD process is fully conformal and operates at room temperature, ensuring compatibility with delicate substrates. The resulting plasma polymers exhibit enhanced long-term environmental stability compared to the original FePc molecule, making them highly suitable for durable energy storage applications. Notably, the FePc30W@CNFs system delivers a specific capacitance nearly 9.5 times higher than that of the $FePc_{sublimated}$@CNFs electrode, a result attributed to the preservation of Fe–N electroactive centres, the incorporation of nitrogen-rich functionalities, and the formation of a conductive and mechanically stable coating that retains structural integrity without demetalation or irreversible degradation under repeated charge–discharge cycling. The assembled symmetric device based on FePc30W@CNFs delivered a high energy density of 7.42 Wh kg^{-1} at a specific power of 225 W kg^{-1} and retained 0.85 Wh kg^{-1} at 6000 W kg^{-1}, with excellent cycling

stability (86.5% retention after 6000 cycles at 0.25 A g^{-1}). This work demonstrates that remote plasma polymerization constitutes an effective route to produce electrodes exhibiting high energy and fast power delivery, establishing RPAVD as a robust strategy for engineering durable phthalocyanine-based supercapacitors. These findings open new avenues for the scalable design of molecularly engineered electrodes, positioning plasma-assisted polymerization as a versatile platform for next-generation energy storage technologies.

Conflicts of interest

There are no conflicts to declare.

Data availability

The data that support the findings of this study are available from the corresponding author upon reasonable request.

Supplementary information (SI) is available. See DOI: https://doi.org/10.1039/d6ta02609e.

Acknowledgements

We are thankful for the projects PID2022-143120OB-I00 and PCI2024-153451 funded by MCIN/AEI/10.13039/501100011033 and by "ERDF (FEDER) a way of making Europe, the Fondos NextgenerationEU and Plan de Recuperación, Transformación y Resiliencia "Project ANGSTROM was selected in the Joint Transnational Call 2023 of M-ERA.NET 3, an EU funded network of about 49 funding organizations (Horizon 2020 grant agreement No. 958174). M. T. acknowledges the funding provided by UK Research and Innovation for EPSRC post doctoral fellowship no. UKRI913. A. J. S. acknowledges the UK Research and Innovation for Future Leaders Fellowship no. MR/T041412/1.

References

1 J. Zhang, M. Gu and X. Chen, Supercapacitors for Renewable Energy Applications: A Review, *Micro Nano Eng.*, 2023, **21**, 100229, DOI: 10.1016/j.mne.2023.100229.

2 K. Dissanayake and D. Kularatna-Abeywardana, A Review of Supercapacitors: Materials, Technology, Challenges, and Renewable Energy Applications, *J. Energy Storage*, 2024, **96**, 112563, DOI: 10.1016/j.est.2024.112563.

3 N. Singh, V. Singh, N. Bisht, P. Negi, A. Dhyani, R. K. Sharma and B. S. Tewari, A Comprehensive Review on Supercapacitors: Basics to Recent Advancements, *J. Energy Storage*, 2025, **121**, 116498, DOI: 10.1016/j.est.2025.116498.

4 E. Vessally, R. M. Rzayev, A. A. Niyazova, T. Aggarwal and K. E. Rahimova, Overview of Recent Developments in Carbon-Based Nanocomposites for Supercapacitor Applications, *RSC Adv.*, 2024, **14**(54), 40141–40159, DOI: 10.1039/D4RA08446B.

5 Y. A. Kumar, R. M. N. Kalla, R. Khan, A. G. Al-Sehemi, A. Ghosh, T. Ramachandran and J. Lee, Double-Transition Metal MXenes for Energy Storage and Conversion Applications, *J. Power Sources*, 2026, **665**, 239027, DOI: 10.1016/j.jpowsour.2025.239027.

6 T. Ramachandran, N. P. Reddy, A. M. Fouda, H. H. Hegazy, A. Maity, P. Ramakrishna, S. S. Rao and Y. A. Kumar, Graphdiyne: A Rising Star in Carbon-Based 2D Materials for Energy and Sensing, *J. Power Sources*, 2026, **677**, 239925, DOI: 10.1016/j.jpowsour.2026.239925.

7 F. Ahmad, A. Shahzad, M. Danish, M. Fatima, M. Adnan, S. Atiq, M. Asim, M. A. Khan, Q. U. Ain and R. Perveen, Recent Developments in Transition Metal Oxide-Based Electrode Composites for Supercapacitor Applications, *J. Energy Storage*, 2024, **81**, 110430, DOI: 10.1016/j.est.2024.110430.

8 V. J. V. Vinayak, K. Deshmukh, V. R. K. Murthy and S. K. K. Pasha, Conducting Polymer Based Nanocomposites for Supercapacitor Applications: A Review of Recent Advances, Challenges and Future Prospects, *J. Energy Storage*, 2024, **100**, 113551, DOI: 10.1016/j.est.2024.113551.

9 W. Ding, L. Xiao, L.-P. Lv and Y. Wang, Redox-Active Organic Electrode Materials for Supercapacitors, *Batter. Supercaps*, 2023, **6**(11), e202300278, DOI: 10.1002/batt.202300278.

10 A. Alharbi, Boosting Supercapacitor Performance through Innovative Transition Metal-Based Electrode Materials, *RSC Adv.*, 2025, **15**(41), 34551–34582, DOI: 10.1039/D5RA02905H.

11 S. Mahala, K. Khosravinia and A. Kiani, Unwanted Degradation in Pseudocapacitors: Challenges and Opportunities, *J. Energy Storage*, 2023, **67**, 107558, DOI: 10.1016/j.est.2023.107558.

12 S. M. S. M. Rahat, K. M. Z. Hasan, M. M. H. Mondol and A. K. Mallik, A Comprehensive Review of Carbon Nanotube-Based Metal Oxide Nanocomposites for Supercapacitors, *J. Energy Storage*, 2023, **73**, 108847, DOI: 10.1016/j.est.2023.108847.

13 S. A. Balogun, S. Mokethe, D. Masekela, D. Thole, D. M. Teffu, A. A. Moronkola, K. Makgopa and K. D. Modibane, Engineering CoPcMWCNTs and NiPcMWCNTs Nanocomposites for Photocatalytic Hydrogen Production and Supercapacitor Applications, *Int. J. Hydrogen Energy*, 2025, **176**, 151494, DOI: 10.1016/j.ijhydene.2025.151494.

14 J. Oni and K. I. Ozoemena, Phthalocyanines in Batteries and Supercapacitors, *J. Porphyrins Phthalocyanines*, 2012, **16**(07n08), 754–760, DOI: 10.1142/S1088424612300078.

15 O. Gorduk, M. Gencten, S. Gorduk, M. Sahin and Y. Sahin, Electrochemical Fabrication and Supercapacitor Performances of Metallo Phthalocyanine/Functionalized-Multiwalled Carbon Nanotube/Polyaniline Modified Hybrid Electrode Materials, *J. Energy Storage*, 2021, **33**, 102049, DOI: 10.1016/j.est.2020.102049.

16 M. A. Deyab, Q. Mohsen and E. Slavcheva, Co-Phthalocyanin/CNTs Nanocomposites: Synthesis, Characterizations, and Application as an Efficient Supercapacitor, *J. Mol. Liq.*, 2022, **359**, 119319, DOI: 10.1016/j.molliq.2022.119319.

17 A. Sanchez-Sanchez, M. T. Izquierdo, S. Mathieu, J. Ghanbaja, A. Celzard and V. Fierro, Structure and Electrochemical Properties of Carbon Nanostructures

Derived from Nickel(II) and Iron(II) Phthalocyanines, *J. Adv. Res.*, 2020, **22**, 85–97, DOI: 10.1016/j.jare.2019.11.004.

18 Q. Wang, H. Gao, C. Zhao, S. Wang, X. Liu, Z. Wang, J. Yu, Y.-U. Kwon and Y. Zhao, π-π Stacked Iron (II) Phthalocyanine/Graphene Oxide Composites: Rational Fabrication and Excellent Supercapacitor Properties with Superior Rate Performance, *J. Solid State Electrochem.*, 2021, **25**(2), 659–670, DOI: 10.1007/s10008-020-04840-7.

19 T. M. Khan, Chapter 15 - Plasma Technology for Supercapacitors, in *Energy from Plasma*, ed. Yasin, G., Nguyen, D. B., Gupta, R. K., Ajmal, S. and Nguyen, T. A., Woodhead Publishing, 2025; pp. 433–463. DOI: 10.1016/B978-0-443-26584-6.00015-4.

20 X. Liang, P. Liu, Z. Qiu, S. Shen, F. Cao, Y. Zhang, M. Chen, X. He, Y. Xia, C. Wang, W. Wan, J. Zhang, H. Huang, Y. Gan, X. Xia and W. Zhang, Plasma Technology for Advanced Electrochemical Energy Storage, *Chem. –Eur. J.*, 2024, **30**(19), e202304168, DOI: 10.1002/chem.202304168.

21 S. Sahoo, G. Sahoo, S. M. Jeong and C. S. Rout, A Review on Supercapacitors Based on Plasma Enhanced Chemical Vapor Deposited Vertical Graphene Arrays, *J. Energy Storage*, 2022, **53**, 105212, DOI: 10.1016/j.est.2022.105212.

22 F. Liu, L.-H. Zhang, Z. Zhang, Y. Zhou, Y. Zhang, J.-L. Huang and Z. Fang, The Application of Plasma Technology for the Preparation of Supercapacitor Electrode Materials, *Dalton Trans.*, 2024, **53**(13), 5749–5769, DOI: 10.1039/D3DT04362B.

23 J. M. Obrero-Perez, L. Contreras-Bernal, F. Nuñez-Galvez, J. Castillo-Seoane, K. Valadez-Villalobos, F. J. Aparicio, J. A. Anta, A. Borras, J. R. Sanchez-Valencia and A. Barranco, Ultrathin Plasma Polymer Passivation of Perovskite Solar Cells for Improved Stability and Reproducibility, *Adv. Energy Mater.*, 2022, **12**(32), 2200812, DOI: 10.1002/aenm.202200812.

24 J. M. Obrero, G. P. Moreno-Martinez, T. C. Rojas, F. J. Ferrer, F. G. Moscoso, L. Contreras-Bernal, J. Castillo-Seoane, F. Nuñez-Galvez, F. J. Aparicio Rebollo, A. Borras, J. R. Sanchez-Valencia and A. Barranco, Enhanced Luminous Transmission and Solar Modulation in Thermochromic VO2 Aerogel-like Films via Remote Plasma Deposition, *ACS Appl. Mater. Interfaces*, 2025, **17**(39), 55172–55188, DOI: 10.1021/acsami.5c07264.

25 J. M. Obrero, L. Contreras-Bernal, F. J. Aparicio Rebollo, T. C. Rojas, F. J. Ferrer, N. Orozco, Z. Saghi, T. Czermak, J. M. Pedrosa, C. López-Santos, K. K. Ostrikov, A. Borras, J. R. Sánchez-Valencia and A. Barranco, Conformal TiO2 Aerogel-Like Films by Plasma Deposition: From Omniphobic Antireflective Coatings to Perovskite Solar Cell Photoelectrodes, *ACS Appl. Mater. Interfaces*, 2024, **16**(30), 39745–39760, DOI: 10.1021/acsami.4c00555.

26 J. M. Obrero-Perez, F. Nuñez-Galvez, L. Contreras-Bernal, J. Castillo-Seoane, G. P. Moreno, T. Czermak, F. J. Aparicio, T. C. Rojas, F. J. Ferrer, A. Borras, A. Barranco and J. R. Sánchez-Valencia, Low-Temperature Remote Plasma Synthesis of Highly Porous TiO2 as Electron Transport Layers in Perovskite Solar Cells, *Adv. Mater. Interfaces*, 2025, **12**(21), e00241, DOI: 10.1002/admi.202500241.

27 M. Nabil, L. Contreras-Bernal, G. P. Moreno-Martinez, J. Obrero-Perez, J. Castillo-Seoane, J. A. Anta, G. Oskam, P. Pistor, A. Borrás, J. R. Sanchez-Valencia and A. Barranco, Boosting Perovskite Solar Cell Stability: Dual Protection with Ultrathin Plasma Polymer Passivation Layers, *Mater. Today Energy*, 2025, **54**, 102117, DOI: 10.1016/j.mtener.2025.102117.

28 F. J. Aparicio, M. Holgado, A. Borras, I. Blaszczyk-Lezak, A. Griol, C. A. Barrios, R. Casquel, F. J. Sanza, H. Sohlström, M. Antelius, A. R. González-Elipe and A. Barranco, Transparent Nanometric Organic Luminescent Films as UV-Active Components in Photonic Structures, *Adv. Mater.*, 2011, **23**(6), 761–765, DOI: 10.1002/adma.201003088.

29 M. C. Biesinger, B. P. Payne, A. P. Grosvenor, L. W. M. Lau, A. R. Gerson and R. S. C. Smart, Resolving Surface Chemical States in XPS Analysis of First Row Transition Metals, Oxides and Hydroxides: Cr, Mn, Fe, Co and Ni, *Appl. Surf. Sci.*, 2011, **257**(7), 2717–2730, DOI: 10.1016/j.apsusc.2010.10.051.

30 L. H. Grey, H.-Y. Nie and M. C. Biesinger, Defining the Nature of Adventitious Carbon and Improving Its Merit as a Charge Correction Reference for XPS, *Appl. Surf. Sci.*, 2024, **653**, 159319, DOI: 10.1016/j.apsusc.2024.159319.

31 M. Alcaire, F. J. Aparicio, J. Obrero, C. López-Santos, F. J. Garcia-Garcia, J. R. Sánchez-Valencia, F. Frutos, K. Ostrikov, A. Borrás and A. Barranco, Plasma Enabled Conformal and Damage Free Encapsulation of Fragile Molecular Matter: From Surface-Supported to On-Device Nanostructures, *Adv. Funct. Mater.*, 2019, **29**, 1903535, DOI: 10.1002/adfm.201903535.

32 J. M. Obrero, A. N. Filippin, M. Alcaire, J. R. Sanchez-Valencia, M. Jacob, C. Matei, F. J. Aparicio, M. Macias-Montero, T. C. Rojas, J. P. Espinos, Z. Saghi, A. Barranco and A. Borras, Supported Porous Nanostructures Developed by Plasma Processing of Metal Phthalocyanines and Porphyrins, *Front. Chem.*, 2020, **8**, 520, DOI: 10.3389/fchem.2020.00520.

33 A. Zanguina, M. Bayo-Bangoura, K. Bayo and G. V. Ouedraogo, IR and UV-Visible spectra of iron (II) phthalocyanine complexes with phosphine or phosphite, *Bull. Chem. Soc. Ethiop.*, 2002, **16**(1), 73–79, DOI: 10.4314/bcse.v16i1.20950.

34 T. Islam, N. Helsel and P. Choudhury, Facile Synthesis of Iron Phthalocyanine Functionalized B-Doped Graphene Composite Using a Green Solvent for Superior ORR Performance, *Mol. Catal.*, 2025, **587**, 115500, DOI: 10.1016/j.mcat.2025.115500.

35 A. Barranco, F. Aparicio, A. Yanguas-Gil, P. Groening, J. Cotrino and A. R. González-Elipe, Optically Active Thin Films Deposited by Plasma Polymerization of Dye Molecules, *Chem. Vap. Deposition*, 2007, **13**, 319–325, DOI: 10.1002/cvde.200606552.

36 J. F. Myers, G. W. R. Canham and A. B. P. Lever, Higher Oxidation Level Phthalocyanine Complexes of Chromium, Iron, Cobalt and Zinc. Phthalocyanine Radical Species,

Inorg. Chem., 1975, **14**(3), 461–468, DOI: 10.1021/ic50145a002.

37 C. J. Ziegler and V. N. Nemykin, The Fascinating Story of Axial Ligand Dependent Spectroscopy and Redox-Properties in Iron(Ii) Phthalocyanines, *Dalton Trans.*, 2023, **52**(43), 15647–15655, DOI: 10.1039/D3DT02565A.

38 W. Li, M. Xiao, J. Jiang, Y. Li, X. Zhang, S. Li, X. Lin, D. Peng, S. W. Or, S. Sun and Z. Xing, Co4N Nanoparticles Embedded in N-Doped Carbon Pores: Advanced Interlayer Material for Lithium-Sulfur Batteries, *Nano Energy*, 2025, **142**, 111140, DOI: 10.1016/j.nanoen.2025.111140.

39 M. W. Thielke, S. Lopez Guzman, J. P. Victoria Tafoya, E. García Tamayo, C. I. Castro Herazo, O. Hosseinaei and A. J. Sobrido, Full Lignin-Derived Electrospun Carbon Materials as Electrodes for Supercapacitors, *Front. Mater.*, 2022, **9**, 859872, DOI: 10.3389/fmats.2022.859872.

40 M. Kakihana, and M. Osada, Chapter 18 - Raman Spectroscopy as a Characterization Tool for Carbon Materials, in *Carbon Alloys*, ed. Yasuda, E., Inagaki, M., Kaneko, K., Endo, M., Oya, A. and Tanabe, Y., Elsevier Science, Oxford, 2003, pp. 285–298. DOI: 10.1016/B978-008044163-4/50018-8.

41 W. Li, M. Xiao, J. Jiang, Y. Li, X. Zhang, S. Li, X. Lin, D. Peng, S. W. Or, S. Sun and Z. Xing, Co4N Nanoparticles Embedded in N-Doped Carbon Pores: Advanced Interlayer Material for Lithium-Sulfur Batteries, *Nano Energy*, 2025, **142**, 111140, DOI: 10.1016/j.nanoen.2025.111140.

42 X. Liu, J. Choi, Z. Xu, C. P. Grey, S. Fleischmann and A. C. Forse, Raman Spectroscopy Measurements Support Disorder-Driven Capacitance in Nanoporous Carbons, *J. Am. Chem. Soc.*, 2024, **146**(45), 30748–30752, DOI: 10.1021/jacs.4c10214.

43 Z. Chen, S. Jiang, G. Kang, D. Nguyen, G. C. Schatz and R. P. Van Duyne, Operando Characterization of Iron Phthalocyanine Deactivation during Oxygen Reduction Reaction Using Electrochemical Tip-Enhanced Raman Spectroscopy, *J. Am. Chem. Soc.*, 2019, **141**(39), 15684–15692, DOI: 10.1021/jacs.9b07979.

44 Z. Liu, X. Zhang, Y. Zhang and J. Jiang, Theoretical Investigation of the Molecular, Electronic Structures and Vibrational Spectra of a Series of First Transition Metal Phthalocyanines, *Spectrochim. Acta, Part A Mol. Biomol. Spectrosc.*, 2007, **67**(5), 1232–1246, DOI: 10.1016/j.saa.2006.10.013.

45 D. R. Tackley, G. Dent, E. Smith and W. Phthalocyanines, Structure and Vibrations, *Phys. Chem. Chem. Phys.*, 2001, **3**(8), 1419–1426, DOI: 10.1039/B007763L.

46 M. Szybowicz and J. Makowiecki, Orientation Study of Iron Phthalocyanine (FePc) Thin Films Deposited on Silicon Substrate Investigated by Atomic Force Microscopy and Micro-Raman Spectroscopy, *J. Mater. Sci.*, 2012, **47**(3), 1522–1530, DOI: 10.1007/s10853-011-5940-7.

47 N. Hellgren, R. T. Haasch, S. Schmidt, L. Hultman and I. Petrov, Interpretation of X-Ray Photoelectron Spectra of Carbon-Nitride Thin Films: New Insights from in Situ XPS, *Carbon*, 2016, **108**, 242–252, DOI: 10.1016/j.carbon.2016.07.017.

48 N. Komba, G. Zhang, Q. Wei, X. Yang, J. Prakash, R. Chenitz, F. Rosei and S. Sun, Iron (II) Phthalocyanine/N-Doped Graphene: A Highly Efficient Non-Precious Metal Catalyst for Oxygen Reduction, *Int. J. Hydrogen Energy*, 2019, **44**(33), 18103–18114, DOI: 10.1016/j.ijhydene.2019.05.032.

49 K. Chen, K. Liu, P. An, H. Li, Y. Lin, J. Hu, C. Jia, J. Fu, H. Li, H. Liu, Z. Lin, W. Li, J. Li, Y.-R. Lu, T.-S. Chan, N. Zhang and M. Liu, Iron Phthalocyanine with Coordination Induced Electronic Localization to Boost Oxygen Reduction Reaction, *Nat. Commun.*, 2020, **11**(1), 4173, DOI: 10.1038/s41467-020-18062-y.

50 Q. Sun, Z. Wang, M. Zhou, J. Li, R. Lu, Y. Wang, X. Liao and Y. Zhao, Tailoring Activity of Iron Phthalocyanine by Edge-Nitrogen Sites Induced Electronic Delocalization, *Appl. Surf. Sci.*, 2023, **624**, 157154, DOI: 10.1016/j.apsusc.2023.157154.

51 R. K. Sahu, D. Mukherjee, J. P. Tiwari, T. Mishra, S. K. Roy and L. C. Pathak, Influence of Foreign Fe Ions on Wet Chemical Synthesis of Pt Nanoparticle Thin Films at Ambient Temperature: In Situversus Direct Addition, *J. Mater. Chem.*, 2009, **19**(37), 6810–6815, DOI: 10.1039/B908080E.

52 A. Paul, S. Ghosh, H. Kolya, C.-W. Kang, N. C. Murmu and T. Kuila, New Insight into the Effect of Oxygen Vacancies on Electrochemical Performance of Nickel-Tin Oxide/Reduced Graphene Oxide Composite for Asymmetric Supercapacitor, *J. Energy Storage*, 2023, **62**, 106922, DOI: 10.1016/j.est.2023.106922.

53 H. Wang, N. Mi, S. Sun, W. Zhang and S. Yao, Oxygen Vacancies Enhancing Capacitance of MgCo2O4 for High Performance Asymmetric Supercapacitors, *J. Alloys Compd.*, 2021, **869**, 159294, DOI: 10.1016/j.jallcom.2021.159294.

54 T. Marshall-Roth, N. J. Libretto, A. T. Wrobel, K. J. Anderton, M. L. Pegis, N. D. Ricke, T. V. Voorhis, J. T. Miller and Y. Surendranath, A Pyridinic Fe-N4 Macrocycle Models the Active Sites in Fe/N-Doped Carbon Electrocatalysts, *Nat. Commun.*, 2020, **11**(1), 5283, DOI: 10.1038/s41467-020-18969-6.

55 M. G. Olayo, E. J. Alvarado, M. González-Torres, L. M. Gómez and G. J. Cruz, Quantifying Amines in Polymers by XPS, *Polym. Bull.*, 2024, **81**(3), 2319–2328, DOI: 10.1007/s00289-023-04829-y.

56 M. H. Kanani-Jazi and S. Akbari, Quantitative XPS Analysis of Amine-Terminated Dendritic Functionalized Halloysite Nanotubes Decorated on PAN Nanofibrous Membrane and Adsorption/Filtration of Cr(VI), *Chem. Eng. J.*, 2024, **482**, 148746, DOI: 10.1016/j.cej.2024.148746.

57 M. Kehrer, J. Duchoslav, A. Hinterreiter, M. Cobet, A. Mehic, T. Stehrer and D. Stifter, XPS Investigation on the Reactivity of Surface Imine Groups with TFAA, *Plasma Processes Polym.*, 2019, **16**(4), 1800160, DOI: 10.1002/ppap.201800160.

58 M. Giesbers, A. T. M. Marcelis and H. Zuilhof, Simulation of XPS C1s Spectra of Organic Monolayers by Quantum Chemical Methods, *Langmuir*, 2013, **29**(15), 4782–4788, DOI: 10.1021/la400445s.

59 P. Zhang, M. Wang, Y. Liu, Y. Fu, M. Gao, G. Wang, F. Wang, Z. Wang, G. Chen, S. Yang, Y. Liu, R. Dong, M. Yu, X. Lu and

X. Feng, Largely Pseudocapacitive Two-Dimensional Conjugated Metal–Organic Framework Anodes with Lowest Unoccupied Molecular Orbital Localized in Nickel-Bis(Dithiolene) Linkages, *J. Am. Chem. Soc.*, 2023, **145**(11), 6247–6256, DOI: 10.1021/jacs.2c12684.

60 Y. Lu, X. Pang, M. Li, M. Liang, W. Wang, Q. He, A. Qahramon Zarifzoda and F. Chen, In-Situ Preparation of Iron(II)-Phthalocyanine@multi-Walled-CNTs Nanocomposite for Quasi-Solid-State Flexible Symmetric Supercapacitors with Long Cycling Life, *ChemSusChem*, 2025, **18**(5), e202401940, DOI: 10.1002/cssc.202401940.

61 R. Raavi, S. Archana, P. Adinarayana Reddy and P. Elumalai, Performances of Dual Carbon Multi-Ion Supercapacitors in Aqueous and Non-Aqueous Electrolytes, *Energy Adv.*, 2023, **2**(3), 385–397, DOI: 10.1039/D2YA00271J.

62 Y. Sun, D. Xu, Z. He, Z. Zhang, L. Fan and S. Wang, Green Fabrication of Pore-Modulated Carbon Aerogels Using a Biological Template for High-Energy Density Supercapacitors, *J. Mater. Chem. A*, 2023, **11**(37), 20011–20020, DOI: 10.1039/D3TA04486F.

63 X. Wei, B. Qiu, H. Tian, Y. Lv, W. Zhang, Q. Qin, Z. Liu and F. Wei, Co-Precipitation Reaction: A Facile Strategy for Designing Hierarchical Porous Carbon Nanosheets for EDLCs and Zinc-Ion Hybrid Supercapacitors, *Appl. Surf. Sci.*, 2023, **615**, 156280, DOI: 10.1016/j.apsusc.2022.156280.

64 T. Ramachandran, M. P. Pachamuthu, R. K. Raji and F. R. M. S. Raj, A Layered Fe–SnO2/MXene Nanohybrid with 1225.6 F G−1 Capacitance and Long-Term Cycle Durability, *Mater. Chem. Phys.*, 2026, **350**, 131860, DOI: 10.1016/j.matchemphys.2025.131860.

65 A. M. Bogale, T. Ramachandran, M. E. Suk, B. B. Badassa, M. M. Solomon, J. He, A. Yusuf, R. K. Raji, B. A. Zenebe, N. K. Amare and F. B. Tesema, Boosted Charge Storage in Symmetric Supercapacitors Using Zn–Co/MgCo2O4 Hybrid Nanosheets, *J. Phys. Chem. Solids*, 2026, **208**, 113079, DOI: 10.1016/j.jpcs.2025.113079.

66 H. Pan, X. Jiao, W. Zhang, L. Fan, Z. Yuan and C. Zhang, Supercapacitor with Ultra-High Power and Energy Density Enabled by Nitrogen/Oxygen-Doped Interconnected Hollow Carbon Nano-Onions, *Chem. Eng. J.*, 2024, **484**, 149663, DOI: 10.1016/j.cej.2024.149663.

67 Y.-J. Gu, W. Wen and J.-M. Wu, Simple Air Calcination Affords Commercial Carbon Cloth with High Areal Specific Capacitance for Symmetrical Supercapacitors, *J. Mater. Chem. A*, 2018, **6**(42), 21078–21086, DOI: 10.1039/C8TA07561A.

68 Q. Wu, T. He, Y. Zhang, J. Zhang, Z. Wang, Y. Liu, L. Zhao, Y. Wu and F. Ran, Cyclic Stability of Supercapacitors: Materials, Energy Storage Mechanism, Test Methods, and Device, *J. Mater. Chem. A*, 2021, **9**(43), 24094–24147, DOI: 10.1039/D1TA06815F.

69 A. Ch. Lazanas and M. I. Prodromidis, Electrochemical Impedance Spectroscopy—A Tutorial, *ACS Meas. Sci. Au*, 2023, **3**(3), 162–193, DOI: 10.1021/acsmeasuresciau.2c00070.

70 M. Z. Iqbal, M. M. Faisal and S. R. Ali, Integration of Supercapacitors and Batteries towards High-Performance Hybrid Energy Storage Devices, *Int. J. Energy Res.*, 2021, **45**(2), 1449–1479, DOI: 10.1002/er.5954.

71 L. Caracciolo, L. Madec and H. Martinez, XPS Analysis of K-Based Reference Compounds to Allow Reliable Studies of Solid Electrolyte Interphase in K-Ion Batteries, *ACS Appl. Energy Mater.*, 2021, **4**(10), 11693–11699, DOI: 10.1021/acsaem.1c02400.

72 L.-L. Chang, C. Hu, C.-C. Huang, C.-Y. Lin, P.-W. Chung and K.-L. Tung, Potassium Citrate-Activated Porous Carbon Nanostructures for CO2 Adsorption and Electroreduction, *ACS Appl. Nano Mater.*, 2023, **6**(10), 8839–8848, DOI: 10.1021/acsanm.3c01231.

73 C. A. Melendres, C. B. Rios, X. Feng and R. McMasters, In Situ Laser Raman Spectra of Iron Phthalocyanine Adsorbed on Copper and Gold Electrodes, *J. Phys. Chem.*, 1983, **87**(18), 3526–3531, DOI: 10.1021/j100241a033.

74 A. Dong, Y. Lin, Y. Guo, D. Chen, X. Wang, Y. Ge, Q. Li and J. Qian, Immobilization of Iron Phthalocyanine on MOF-Derived N-Doped Carbon for Promoting Oxygen Reduction in Zinc-Air Battery, *J. Colloid Interface Sci.*, 2023, **650**, 2056–2064, DOI: 10.1016/j.jcis.2023.06.043.

75 M. Chattanahalli Devendrachari, G. Shimoga, S.-H. Lee, Y.-H. Heo, H. Makri Nimbegondi Kotresh, R. R. Palem, S.-Y. Kim and D.-S. Choi, Advancing Energy Storage Competence through Copper Phthalocyanine-Stabilized Titanium Nitride Hybrid Nanocomposites for Symmetric Supercapacitors, *ACS Appl. Energy Mater.*, 2023, **6**(21), 11199–11211, DOI: 10.1021/acsaem.3c02093.

76 D. Han, W. Wang, S. Yu, W. Qi, R. Ling, C. Yang and G. Liu, Stable β-Form Zinc Phthalocyanine Cathodes for Flexible Zn-Ion Hybrid Supercapacitors with Ultra-Long Cycling Life, *Chem. Eng. J.*, 2023, **468**, 143875, DOI: 10.1016/j.cej.2023.143875.

77 K. P. Madhuri and N. S. John, Supercapacitor Application of Nickel Phthalocyanine Nanofibres and Its Composite with Reduced Graphene Oxide, *Appl. Surf. Sci.*, 2018, **449**, 528–536, DOI: 10.1016/j.apsusc.2017.12.021.

78 C. Du, J. L. Chen-Qiu, Z. Zhao, F. Zamora and H. Liu, Recent Progress in Supercapacitors: A Critical Review of Energy Storage Mechanisms, Electrode Design Strategies and Future Perspectives, *J. Alloys Compd.*, 2026, **1054**, 186363, DOI: 10.1016/j.jallcom.2026.186363.

79 X. Fang, U. Falak, A. Rasheed, G. Dastgeer, O. Ruzimuradov, S. Mamatkulov, K. Butanov, K. Saidov, D. J. Kang, H. Zhang, S. G. Lee and W. He, Recent Advances in Fibre-Shaped Supercapacitors for Flexible and Wearable Energy-Storage Applications, *Chem. Mater.*, 2026, **38**(2), 586–606, DOI: 10.1021/acs.chemmater.5c02828.

